PARALLEL BLADE–VORTEX INTERACTION

M. C. WILDER† AND D. P. TELIONIS

*Department of Engineering Science and Mechanics, Virginia Polytechnic Institute and State
University, Blacksburg, VA 24061-0219, U.S.A.*

Laser–Doppler velocimetry was employed to experimentally investigate two-dimensional
airfoil– vortex interaction. Vortices were generated by sinusoidally oscillating a NACA 0012
airfoil about its quarter-chord at a reduced frequency of $k = 2\cdot05$ and an amplitude of $\pm\,10°$
in angle of attack. The target airfoil, a NACA 63_2A015 was immersed in the wake, two chord
lengths downstream of the vortex generator's trailing edge. Phase-averaged velocity
measurements of the flow around the target airfoil were made with the latter at angles of
attack of $\alpha = 0°$ (unloaded blade) and $\alpha = 10°$ (loaded blade). A close encounter with
a counterclockwise rotating vortex was studied for both angles of attack and a head-on
collision which splits the counterclockwise rotating vortex in two was investigated for
$\alpha = 10°$. Vorticity fields were constructed and surface pressure fluctuations on the airfoil
were determined. It was found that the most violent interaction occurs when the disturbing
vortex passes very near over the loaded airfoil. On the other hand, with head-on collision,
the disturbing vortex is split, the pressure spikes are drastically reduced and the vortex
disintegrates. The opportunity arises therefore to unload a blade during the short interval of
vortex interaction, in order to reduce the severity of blade–vortex interaction.

© 1998 Academic Press

1. INTRODUCTION

VORTICITY GENERATED AT THE TIP OF A HELICOPTER ROTOR BLADE rolls up into concentrated
vortices which sustain their character for considerable distances downstream. When these
vortices interact with following rotor blades, the unsteady pressure fluctuations induced on
the solid surfaces lead to severe dynamic structural loading and noise production. The
blade–vortex interaction, (BVI) is the source of the familiar *blade slap* sound of helicopters.

This interaction is an example of a broad class of unsteady fluid dynamics problems
which can be generalized as body–turbulence interaction (Bushnell 1984). The turbulence
field can take any form, from full three-dimensional, uncorrelated turbulence (wind gusts
against structures), to highly coherent, uniform vortices (such as the BVI problem). Any
wing-like surface will shed vorticity at its tip, which can interact with other solid surfaces
further downstream. Examples include turbine rotor wake–stator interaction, propeller
wake-wing or fuselage interaction, and canard–wing interaction.

In some cases, research in helicopter BVI was carried out with rotating model blades.
Caradonna *et al.* (1988) reported unsteady pressure measurements made on a nonlifting
rotor model during blade–vortex interaction. A leading-edge pressure pulse was the domi-
nant feature of the BVI. Detailed velocity measurements in the tip vortex core of a single-
bladed model rotor in hover were made by Thompson *et al.* (1987); however, due to the

---
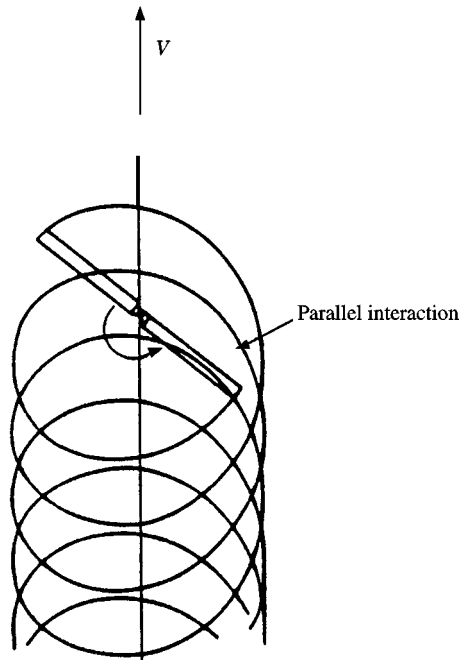
†Present address: MCAT Inc., San José, CA, U.S.A.

Figure 1. Blade–vortex interaction in a helicopter rotor. Top view of an advancing but descending rotor blade. The solid lines emanating from the tips represent the trajectories of the tip vortices.

downwash of the rotor, no blade–vortex interaction occurred in this study. The geometry of the problem is so complex that it is impossible to obtain careful velocity measurements around a rotating blade. The basic underlying features of the flow are therefore only surmised on the basis of surface pressure measurements. In the present contribution, we consider a somewhat simplified problem, which however enables us to study in great detail the features of the flow, namely, parallel blade–vortex interaction.

Blade–vortex interactions within a helicopter rotor system are shown schematically in Figure 1. There are regions in which the vortex core is nearly perpendicular to the blade span and other regions in which the core is nearly parallel. For parallel interaction, the helicopter rotor BVI problems can be modeled in two dimensions, while retaining many of the physical characteristics of the actual interaction. Analytical predictions by Widnall (1971) indicate that parallel interaction produces the largest-amplitude radiated noise pulse. Noise directivity studies (Martin *et al.* 1987) and noise source identification (Splettstoesser *et al.* 1987) bear out this conclusion. For this reason, the helicopter BVI problem has quite often been studied in the form of a two-dimensional parallel interaction and this is the approach adopted here.

Work on the problem of parallel blade–vortex interaction can be grouped into two broad categories. In the first, the emphasis is placed upon the influence that a vortex has on an airfoil (or any body, in general), whereas in the second category, the effect of the interaction on the vortex itself is examined. With the exception of Gursul & Rockwell (1990), most contributions to the problem of airfoil–vortex interaction fall within the first category. Measurements are typically in the form of unsteady surface pressures. The flow fields have been primarily investigated via flow visualization. In the present paper we report on detailed results obtained via laser-Doppler velocimetry and examine problems in both categories.

Preliminary evidence collected so far (Booth & Yu 1986; Caradonna *et al.* 1986; Pesce *et al.* 1991) indicates that direct interaction of a vortex with a blade, that is when a vortex reaches the immediate neighborhood of the leading edge of the blade is not always violent. The following basic question is then posed. What characteristics of the flow lead to significant differences in BVI effects due to only small variations of the parameters that control the phenomenon? Moreover, the pressure signatures observed (Booth & Yu, 1986; Strauss *et al.* 1990) consist usually of multiple oscillations but on occasion, they appear as a single spike. Again, it is not known what type of flow characteristics could generate such behavior. The present effort was undertaken to explore the physics of the flow that give rise to these phenomena.

Hardin & Lamkin (1987a) employed an idealized mathematical model to identify the parameters that control the severity of blade–vortex interaction. Modeling the blade by a single, bound point vortex and the disturbing vortex by a drifting ideal point vortex, they pointed out that BVI acoustic pressure time history is proportional to the product of the bound vortex circulation and the drifting vortex circulation. Inspired by this simple analytical result, Marcolini *et al.* (1995) tested a rotating blade in a wind tunnel and demonstrated that the BVI sound level could indeed be reduced if a blade were to be unloaded for a short portion of its rotation, so that the strength of the disturbing vortex may be weaker during the BVI event. Here we undertook to explore the effect that the loading, i.e., the level of bound circulation has on blade–vortex interaction.

Two-dimensional vortex disturbances can be generated by a variety of methods. Rockwell & Knisely (1979) and Graf & Durgin (1990) made use of the natural instabilities inherent in a free shear layer to investigate vortex impingement upon a corner. Ziada & Rockwell (1982) Kaykayoglu & Rockwell (1985) and Sohn & Rockwell (1987) have also employed mixing layers in the examination of vortex impingement with sharp and elliptical leading edges at zero angle of incidence. But vortices thus generated are small and could not model correctly the ratio of vortex-to-blade circulation of the BVI problem. Unsteady surface pressure measurements, and streakline and timeline flow visualizations were employed in these studies. Rockwell (1984) provides an overview of earlier work of this type.

The vortices naturally formed in the wake of a bluff body have also been used in the study of vortex interaction with a body. The obvious disadvantages of using the von Kármán vortex street are the relatively close vortex spacing and the elevated turbulence due to the dead-air region behind the bluff body. Meier & Timm (1985) employed Mach–Zehnder interferometry to study the interaction of vortices generated by different cylinders with an airfoil. Gursul & Rockwell (1990) studied body–vortex interaction by immersing the body in the wake of shedding plates. Unsteady surface pressures and streakline flow visualizations of the interaction of the vortices with an elliptical leading edge were presented. Gursul & Rockwell also provided detailed laser-Doppler velocity measurements in the leading-edge region. The velocity measurements were used to calculate vorticity and pressure fields, and to simulate streakline and timeline flow visualizations. Meier & Timm (1985) employed vortices generated by an airfoil placed in starting flow in a shock tube. A second airfoil was placed upstream of the test airfoil. The starting vortex shed by the second airfoil had a very small core radius and velocity distribution close to a potential vortex. The experimental results were compared with inviscid calculations using conformal mapping.

Another method of generating a two-dimensional vortex disturbance and the one employed here is by oscillating an airfoil in pitch. Free shear layers shed from the trailing edge of the airfoil as it undergoes rapid changes in angle of attack quickly roll up into large-scale coherent vortical structures. For sinusoidal oscillations, these structures arrange themselves in the form of a street of vortices with alternating rotational sense. This wake is similar in appearance to the Kármán vortex street of bluff bodies, but the rotational sense of

the vortices is opposite to that of the bluff body wake and the field is almost free of turbulence. Booth & Yu (1986) presented smoke flow visualizations for a symmetric airfoil in the wake of a sinusoidally and a nonsinusoidally oscillating airfoil. The nonsinusoidal oscillation waveform consisted of a rapid up-stroke. In this way, only one strong vortex was formed per oscillation period, increasing the separation between vortices by about five times, and isolating each encounter from the effects of the previous ones. Booth (1986) recorded unsteady pressures on the first 20% of the blade surface and later (Booth 1987a, b) computed the far-field noise from the measured surface pressures. Steady and unsteady pressures were measured by Straus et al. (1990) for the interaction of a counterclockwise rotating vortex with a symmetric airfoil at zero angle of incidence. The vortices were formed by pitching a symmetric airfoil about its center of mass. Measured pressures and lift and moment coefficients were compared with pressures computed by the discrete vortex method. Swirydczuk (1990) also employed a nonsinusoidally pitching schedule in order to lengthen the separation between vortices. Smoke-wire visualization was used to examine the interaction of a single vortex with a thin symmetrical airfoil and its wake. The emphasis of this investigation was placed on the vortex–wake interaction. In all these investigations, flow visualization and pressure measurements were made, and little information could be derived on the velocity and vorticity field. Here we give emphasis to the latter, employing laser–Doppler velocimetry.

A variety of numerical simulations of parallel blade–vortex interaction have been reported as well. Methods range from inviscid discrete vortex modeling to numerical solutions of the Euler and Navier–Stokes equations, to exact analytical solutions. Panaras (1987), and Lee & Smith (1987), employed a cloud of discrete vortices in modeling the vortex core. Poling et al. (1989) used a single discrete vortex and conformal mapping analysis with an unsteady Kutta condition to model the airfoil–vortex interaction. They later replaced the vortex with a cloud of vortices to represent an extended vortex core (Poling et al. 1988). Unsteady pressures using the vortex cloud were compared with experimental results (Poling et al. 1991). Inviscid calculations were made by Swirydczuk (1990), Straus et al. (1990), and Meier & Timm (1985) to compare with their experimental results. Hardin & Lamkin (1987) developed an Euler code that predicts the radiated noise due to the interaction of a distributed vortex with a Joukowski airfoil. Wu et al. (1985) used the Euler equations in calculations of compressible inviscid transonic flow, and Lee et al. (1990) used an Euler–Lagrangian method.

The problem of blade–vortex interaction was treated analytically by Jones (1972), who obtained exact analytical solutions based on some simplifying assumptions. Farassat & Succi (1983) developed analytical formulations for predicting radiated helicopter noise. These formulations were employed by Booth (1990) to calculate radiated noise from experimentally obtained surface pressures. Lee & Roberts (1985) computed the impulsive noise due to blade–vortex interaction using an analytical turbulent vortex core model. Hardin & Lamkin (1986) identified the critical parameters controlling noise generation by an analysis of a simplified physical model. They have essentially demonstrated that the radiated noise can be calculated easily in terms of the unsteady pressure distribution on the surface of a solid body. It is therefore necessary to understand the mechanisms involved and provide benchmark data for the flow in the immediate neighborhood of the blade surface and this is the purpose of the present contribution.

The vortex disturbance for the experimental work reported here was generated by oscillating a symmetrical airfoil about its quarter-chord point. A careful survey of the velocity distribution of the vortices and of the repeatability of producing the disturbance was conducted earlier by the group of the present authors (Mathioulakis et al. 1985; Wilder 1992; Wilder et al. 1996). It was found that vortex sheets quickly roll up to form nearly

axisymmetric vortical structures. These structures contain a finite core where vorticity is almost uniformly distributed.

Of all earlier investigators, only Gursul & Rockwell (1990) reported measurements of the developing velocity field and the corresponding vorticity field of a vortex interacting with a rounded nose. They provided the fundamental character of vortex–parabolic nose interaction, observing the distortion of the vortical structures and the corresponding pressure peaks near the tip. Their disturbing vortices were small and of relatively low Reynolds number the direct and as a result, no separation was induced over the tip. The present work extends our understanding of the interaction problem by considering higher Reynolds numbers, stronger vortices with wide cores which induce separation and by considering loaded blades, i.e., blades at an angle of attack, a condition which was found to increase drastically the severity of the interaction. Detailed numerical parameters of vortex characteristics of earlier contributions are presented and compared with the present data in Section 3.

The Reynolds number of the present experiment is still rather low, namely, Re = 19000. However, Wilder et al. (1996) demonstrated experimentally that at this Reynolds number, the shear layers rolling into the large vortical structures are fully turbulent. In the same paper, evidence was provided that indicates that the size, circulation and spacing of these vortices are invariant to the value of the Reynolds number, i.e., to the laminar or turbulent character of the flow. For the Reynolds number tested here, the disturbing vortices are turbulent, but separation over the leading edge is laminar. The present study is presented as a benchmark case, to offer understanding of the mechanisms involved and to provide data for code validation.

The Mach number of the flow studied here is zero. We therefore have no information to offer on the effects of compressibility. Most recent evidence indicates that compressibility at low subsonic Mach numbers reduces somewhat the dynamic effects of unsteady stall (Chandrasekhara et al. 1994) but at higher Mach numbers the pressure spikes for BVI are actually more pronounced (Srinivasan & McCroskey 1993; Meier & Timm 1985).

In the next section, a discussion of the experimental facilities and techniques is offered. An examination of the two dimensionality and repeatability of the flow in the wake of the oscillating airfoil can be found in Wilder (1992). The results of a detailed investigation of the blade-vortex interaction are presented in Section 3. LDV measurements were obtained around the leading edge of the airfoil during the interaction and in a special case around the entire airfoil. Three cases were studied: a close encounter with the airfoil at a zero-degree angle of attack; and both a close encounter and a direct encounter with the airfoil at an angle of attack of 10°.

2. EXPERIMENTAL FACILITIES AND INSTRUMENTATION

2.1. The Water Tunnel and the Model

Tests were conducted in a closed-circuit water tunnel, with a 6:1 two-dimensional contraction, delivering free-stream velocities from about 15 cm/s up to 1·5 m/s. Free-stream turbulence levels at the upstream end of the test section were the order of 0·7% (Koromilas & Telionis 1980). A new test-section was designed and installed to conduct the work described here (Telionis & Wilder 1988). Built of clear plexiglass, the inside cross-section of the test-section is 25 cm (span) × 30 cm, and the length is 244 cm measured from the end of the contraction. The test-section proper, i.e., the segment of the 244 cm-long test-section in which measurements were performed (hereafter referred to simply as the test-section), is a removable plexiglass box. The top and bottom of this box serve as the roof and inner floor
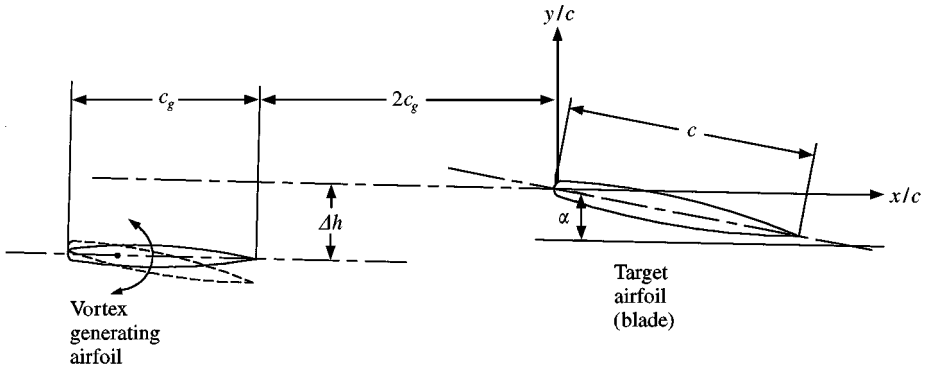
Figure 2. Coordinate system for the airfoil–vortex interaction experiments.

of the water tunnel when in place, while the box walls serve as side (or false) walls to our models. The inside dimensions of the test-section box are 21·5 cm (span) × 30 cm, leaving a 0·95 cm gap between the false walls and the tunnel walls. The false walls are beveled at the leading-edge and act as end-plates for the airfoil models. The test-section box is 48.2 cm long, while the false walls are extended by another 22·8 cm by segments permanently mounted inside the tunnel. Appropriate adjustment of these extensions leads to removal of the side-wall boundary layers.

Vortices were generated by oscillating an airfoil, the "disturbing airfoil" in pitch. The airfoil, a NACA 0012 with a chord length $c_g = 10·16$ cm, was pitched about its quarter-chord by a 3/4-horsepower dc motor. The rotational motion of the motor was translated to a pitching motion of the airfoil via a four-bar linkage system. The target airfoil, also called the "blade", was a NACA 63_2A015 symmetrical airfoil. Its chord length was $c = 15·24$ cm and it spanned the water tunnel test section. The leading edge was placed two vortex-generator chord lengths ($2c_g = 20·32$ cm) downstream of the neutral position ($\alpha = 0°$) of the vortex generator trailing edge, and displaced vertically by an adjustable distance Δh. A schematic of the airfoil arrangement is shown in Figure 2. The blockage ratio at the highest angle of attack tested was 8.8%. The origin of the coordinate system was located at the leading edge of the target airfoil and aligned with the stream.

The data acquisition was coordinated with the oscillating airfoil via an optical trigger (a side-by-side LED-phototransistor pair) mounted beside the flywheel of the pitching mechanism. The reflective tab was positioned so that the triggering pulse occurred as the airfoil began its upstroke, i.e., the airfoil was at $-10°$ angle of attack and was beginning to pitch up. This was defined as the zero time, $t = 0$ for all the motions. Physical characteristics of vortices produced by the oscillating airfoil are described in Mathioulakis et al. (1985), Wilder (1992) and Wilder et al. (1996).

Two laser-Doppler velocimeters were used in this work. A single-component system monitored the free-stream velocity of the water tunnel and a more complex, two-component system was employed in making velocity measurements in the test section. The two-component system was capable of detecting flow reversals and could automatically traverse the measurement volume over a predefined grid. Both systems were controlled by the laboratory computer (MINC-11). The free-stream monitor was a single-component DISA, type 55L laser-Doppler velocimeter which will be referred to here as the DISA LDV or DISA system. Its probe volume was positioned 14 cm downstream of the tunnel contraction and as near to the center of the tunnel cross-section as possible. The free-stream velocity U_∞ was continuously measured and the ratios u/U_∞ and v/U_∞ were obtained on-line,
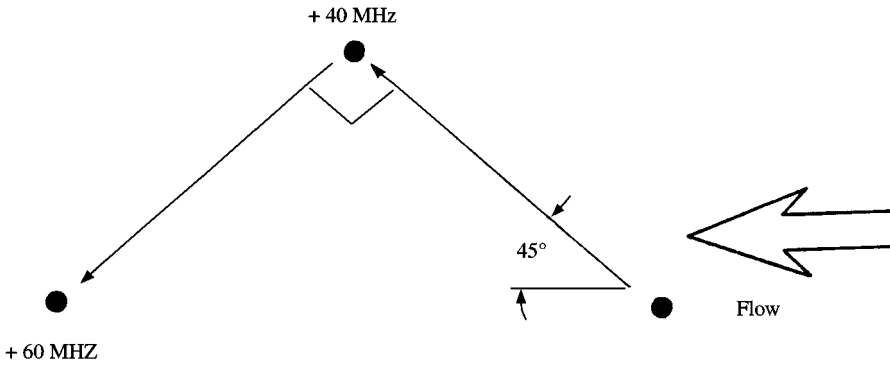
Figure 3. Beam arrangement for the TSI LDV.

thus eliminating low-frequency drifts or the effects of day-to-day variations in the tunnel speed.

The other system, a two-component TSI, He-Ne LDV was the principal instrument in this investigation. Optical components (collectively referred to as the optics train) included a beam collimator, two polarization axis rotators, a pair of beam splitters (prism type), two Bragg cells, beam steering wedges (for fine tuning the alignment), a single photodetector, and a beam expansion unit with a 2·27 expansion ratio. Following the optics train, a pair of mirrors projected the laser beams through a 250 mm $f/4$ lens. This gave a measuring volume with a length of 1.26 mm, a diameter of only 0·089 mm, and a fringe spacing of 4·5 μm. Signals were collected in back-scatter mode, with the transmission optics also serving as the receiving optics. This greatly simplified the traversing of the measuring volume, since the transmission and reception optics move in unison. More details of the experimental rig can be found in Mathioulakis & Telionis (1987, 1989).

Usually, multi-colored beams are employed in multi-component LDV work. The system used here employs a single-color laser and frequency shifting linked with electronic filtering to separate the scattered light signals. The laser beam from a 15 mW He–Ne Spectra Physics laser is split into three equal intensity beams. Two of the beams are frequency-shifted, one by 40 MHz and the other by 60 MHz. The three beams are arranged so as to form the vertices of a 45, 45, 90° triangle as shown in Figure 3. Each beam pair is sensitive to a component of the velocity, however, only two are linearly independent. The two components measured are orthogonal to one another and inclined by $\pm 45°$, to the direction of the free-stream, respectively. One velocity component is measured with the 40–60 MHz beam pair and has a measured frequency of $f_D + 20$ MHz where f_D is the Doppler frequency. The other component uses the 40 MHz-unshifted beam pair. Its frequency is $f_D + 40$ MHz. Both signals are received with the same photodetector and are electronically separated with band-pass filters. After separating the signals, the Bragg cell frequencies are subtracted by electronic down-mixing. Flow reversals are detected by adding an additional frequency shift to the laser beams. This frequency is typically selected to be approximately twice the mean Doppler frequency of the flow, and is not down-mixed from the signals. The signal sent to the signal processors has a frequency equal to f_D + "shift frequency".

Automatic displacement of the measurement volume within a vertical plane was made possible with a pair of stepping motors. Stepping was controlled by the laboratory computer and each motor was equipped with a linear variable differential transducer (LVDT) which acts in a feedback loop to insure accurate positioning of the measurement

volume to within 0·05 mm, (nearly half the measurement volume diameter). Vertical displacement was achieved with mirrors by a device designed and constructed in our laboratory (Mathioulakis & Telionis 1987). For horizontal displacement the entire optical train was displaced. The laser, optics and vertical traversing tower were all mounted on a sliding table which moves parallel to the test-section.

The train of optics was suspended between rotatable mounts. This feature becomes necessary when making measurements near a curved surface, to avoid blocking the beams by the model. Measurements near the leading edge of the airfoil model were facilitated by rotating the optical train. The beams were slightly tilted towards the model surface (tilt angles were between 4 and 6°). Tilting the beams allowed measurements to be made closer to the model surface. More details on these arrangements can be found in Wilder (1992).

2.2. Data Reduction

For purposes of calculating vorticity, the velocity data were smoothed. By plotting isolevel contours of vorticity, we can track the path and evolution of vortices in the wake of the pitching airfoil and their interaction with the fixed airfoil. Unsmoothed velocity data were used in circulation and pressure calculations because the numerical integration involved in these calculations has a similar smoothing effect.

Vorticity was calculated from the measurements by using finite-difference formulae to evaluate the velocity derivatives. Two- and three-point difference formulae were employed, depending on the step size between measurement stations. For example, if the x-step size of the measurements was twice the y-step size ($\Delta x = 2\Delta y$), a two-point formula was used for the x-derivative and a three-point formula for the y-derivative:

$$\Omega(x, y, t) = \frac{v(x + \Delta x, y, t) - v(x, y, t)}{\Delta x} - \frac{u(x, y + \Delta y, t) - u(x, y - \Delta y, t)}{2\Delta y}. \tag{1}$$

This ratio of step sizes is typical for much of the data presented in this text.

Some of the measurements in the wake of the oscillating airfoil were made along single columns in space. Velocity time-records made along a single column (or survey line) can be utilized to construct an instantaneous spatial velocity or vorticity field by assuming that the vortices convect downstream with a constant drifting velocity U_d in a *frozen* pattern. In this situation, an observation made at time t_2 and a distance $U_d\Delta t$ downstream of the measurement station would be equivalent to an observation made at the measurement station at time $t_1 = t_2 - \Delta t$. This field is essentially the time record in reverse order with the spacing between columns equal to $U_d\Delta t$. When calculating vorticity for this type of measurements, the x-derivative is evaluated as

$$\frac{\partial v}{\partial x} \approx \frac{v(y, t) - v(y, t + \Delta t)}{U_d\Delta t}. \tag{2}$$

This is essentially equivalent to Taylor's hypothesis.

In this paper, we introduce an extension of the frozen vorticity assumption, which allows for local distortions of the vortices. Velocity measurements are made along a closely spaced pair of survey lines and the vorticity time record is evaluated according to equation (1). The vorticity field in the neighborhood of the two columns is then constructed from the time record by assuming that, over short distances, viscosity does not influence significantly the motion and thus, vorticity propagates with the local velocity. Moreover, the stretching term is eliminated because of the two-dimensionality of the flow. Vorticity equation is thus

reduced to

$$\frac{D\Omega}{Dt} = 0. \tag{3}$$

It is then assumed that vorticity at a point on the measuring station is convected at the next time step by an increment proportional to the local velocity and in the direction of the local velocity vector. Data along the pair of survey lines are thus used to *open a window* in the flow, to the right and left of the two survey lines. This is essentially a manifestation of the Kelvin–Helmholtz theorem and the procedure can thus be termed a Kelvin extrapolation. The flow in the entire domain of interest can be defined with relatively few measurements, by using several windows. The validity of the method was demonstrated by Wilder (1992) by comparing data obtained along a tight grid to data obtained along a few pairs of columns.

Circulation over a certain domain is calculated either by a line integral over the velocity or by the area integral over vorticity. The line integral is evaluated by repeated applications of the trapezoidal rule and is performed on either circular paths or paths of constant vorticity. Integration proceeds in the counterclockwise direction, so that a vortex with counterclockwise rotation has positive circulation. The area integral is evaluated by summing the vorticity multiplied with the incremental area of the measurement grid. We found it convenient here to define another quantity, sectional circulation, as just the circulation over a narrow vertical strip of width Δx:

$$\Gamma_s = \Delta x \int \Omega \, dy. \tag{4}$$

This quantity therefore represents a slice of the vorticity flux along a fixed vertical section.

A major concern in the study of the airfoil–vortex interaction is the effect of the vortex on the loads experienced by the airfoil. Unsteady surface pressures on the model are determined by evaluating the terms of the Navier–Stokes equations that involve velocity components in terms of the measured quantities, to obtain $\partial p/\partial x$ and $\partial p/\partial y$. The resulting pressure gradients are integrated along x- and y-coordinate lines:

$$p(x, y, t) = p_\infty + \int \left(\frac{\partial p}{\partial x} \, dx + \frac{\partial p}{\partial y} \, dy \right). \tag{5}$$

The assumption is made that the pressure at the measurement location farthest upstream and above the airfoil is equal to the pressure of the free stream, p_∞. Pressures are presented in terms of a nondimensional coefficient,

$$C_p = \left(\frac{p - p_\infty}{\rho U_\infty^2} \right), \tag{6}$$

where U_∞ is the velocity measured upstream by the DISA system.

2.3. UNCERTAINTY ANALYSIS

Since the wavelength of the light emitted by a laser is precisely known, the systematic uncertainty inherent in LDV measurements is due to inaccurate beam alignment and the systematic uncertainty in the measurement of the Doppler frequency. The beam crossing angle was determined by measuring the focal length of the lens and the distance between the laser beams at the plane of the focusing lens. An alignment mask was employed to measure the beam separation. These distances were measured with an estimated accuracy of half a beam diameter, or 0·5 mm. Thus the crossing angle was determined to within 0·1°. The

beam rotation and tilt angles, were measured with similar accuracy. The reader will find more details of this analysis in Wilder (1992).

Next, the systematic uncertainty of measuring the Doppler frequency, introduced through the signal processors and computer analog-to-digital (A/D) converter, was estimated by sampling a signal of known frequency. A sine wave signal was produced with a function generator (Hewlett Packard HP 3311A) and fed to the TSI counters. As a check on the signal generator, the signal was also examined with a frequency counter (HP 5381A) and a dynamic signal analyzer (HP 3562A). The frequency measured by these two devices was within 0·5% of one another. A signal frequency of 130 kHz, equivalent to the mean Doppler frequency typical of the experiments was selected and the adjustments of the TSI counters were set as in the experiments. Adjustments included the input signal filter bandwidths, the timer range and the timer comparison. The analog frequency output of the counters was sent to the computer A/D board, which was sampled for 3 s at a rate of 100 Hz, a typical sampling rate in the experiments. From these samples, the mean frequency and its standard deviation were computed in terms of 300 samples.

The mean frequency for each signal processor differed by less than 0.1% of the source frequency as determined by the HP counter and the sample standard deviation was consistently around 0·05% of the mean. This test was repeated with a source signal of 30 and 100 kHz. The sample standard deviation was again around 0·05%, of the mean, but the mean differed by 0·8% of the source frequency for the lower frequencies. Using these expected errors in the frequency and beam alignment, the uncertainty on the velocity measurements was estimated as $0·027U_\infty$ (Wilder 1992).

Velocity measurements performed in the unsteady wake of the oscillating airfoil were ensemble averaged over many oscillations. The effectiveness of ensemble averaging in reducing the influence of random fluctuations on the free-stream measurements was evaluated by examining velocity histograms. The standard deviation of the free-stream velocity measurements dropped from 1·3 to 0·3% as a result of ensemble averaging.

Velocity measurements were made during M periods of the pitching motion. Each period contained N samples separated in time by the sample interval $\Delta t = T/N$, where T is the period of oscillation. The sample interval is the time between analog-to-digital conversions performed by the laboratory computer. Every Δt seconds, the computer converts the voltage output of the signal processor to a digital value. The seeding particles, however, pass through the LDV measuring volume at random intervals. The laboratory computer employs a sample-and-hold technique in which, if no new signal is output by the LDV signal processor, the last signal is repeatedly sampled every Δt seconds. For low data rates (or high sample rates), this process results in a choppy representation of the periodic fluctuation. In the present experiments, the data rate was sufficiently high so that a few Doppler signals were available within each Δt. By repeating the measurements over several periods and ensemble averaging, the time record is filled in and random fluctuations are averaged out.

To estimate the repeatability of the flow in the wake of the oscillating airfoil, the standard deviation of the measured velocity components was evaluated for each phase of the pitching motion. This phase standard deviation or phase-r.m.s. is defined as

$$\sigma(\phi) = \sqrt{\frac{1}{M-1} \sum_{m=1}^{M} (U_m(\phi) - \bar{U}(\phi))^2}, \tag{7}$$

where the phase $\phi = (t/T)360°$ is a nondimensional time, M is the total number of time records, and $\bar{U}(\phi)$ is the velocity for a given phase averaged over all M time records. Zero time and zero phase is defined arbitrarily as the point at which the disturbing airfoil is at its
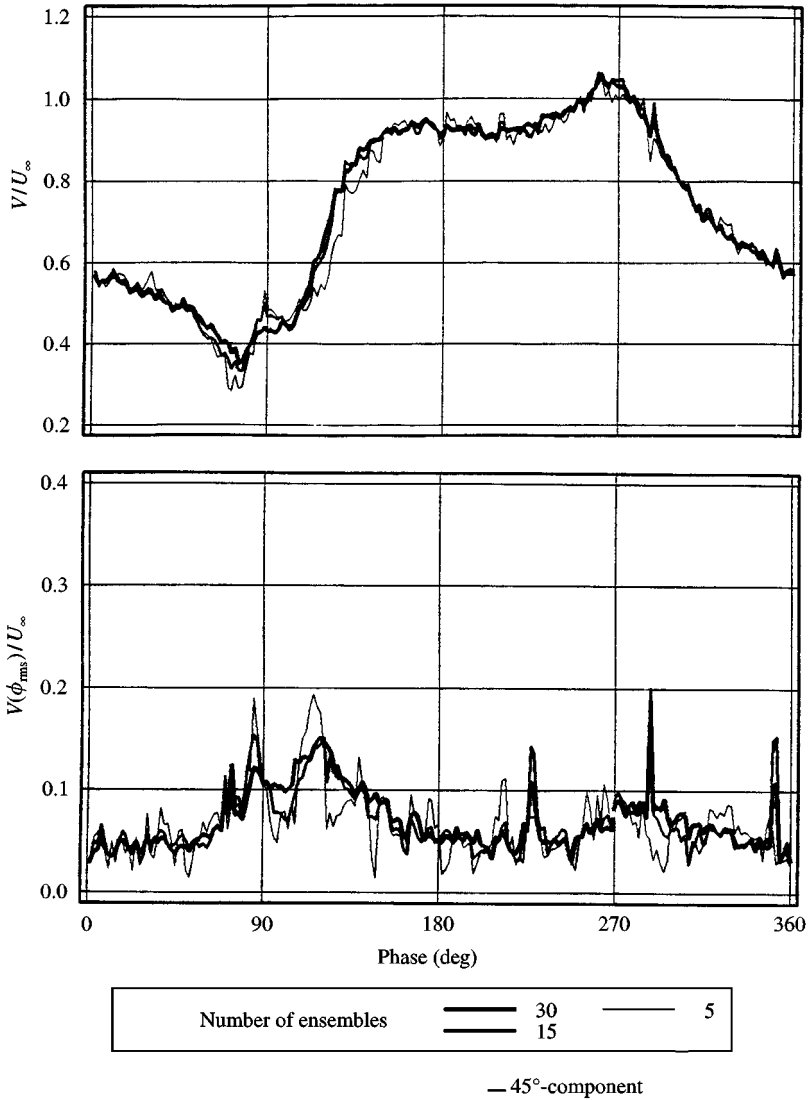
Figure 4. Ensemble-averaged velocity and phase-r.m.s. for 5, 14, and 30 ensembles: $U_\infty = 12.5\,\text{cm/s}$, $k = 2.05$, $x/c_g = 2.0$, $y/c_g = 0.1$.

10°-incidence position. An example of one ensemble-averaged velocity component is presented along with respective phase-r.m.s. (Fig. 4). Shown are the results obtained using 5, 15 and 30 time records. The reduced frequency of the oscillating airfoil was equal to 2.05 and the average free-stream velocity was $U_\infty = 12.5$ cm/s. We see that as few as five records are sufficient to produce a reasonably smooth ensemble average and that, with the exception of certain phase angles, the phase-rms for five and thirty averages are quite similar. This means that with thirty time records we can accurately estimate the phase-wise velocity statistics; namely the ensemble-average velocity and phase-r.m.s. The phase-r.m.s. is maximum around 90 and 270° of phase, when the change in the velocity gradient is maximum (i.e., when a vortex passes the measuring station) It is significant to note that the dominant characteristics of the waveform, i.e., the time of events like sharp changes in the slope are not

affected by averaging. This implies that the disturbances arrive at the measuring station at fixed intervals and therefore the vortices shed by the pitching airfoil follow a repeatable spatial and temporal path.

Typically, 20–30 velocity time records were measured, i.e., $M = 20$ or 30. The time required to run an experiment was a constraint in selecting the number of ensembles to employ. A survey line consisting of 40 measurement stations required about 2 h for completion when 30 time records were obtained. An order of magnitude increase in the number of records was required to improve the velocity statistics. In addition to the period-to-period flow repeatability represented by the phase-r.m.s. (Figure 4), the repeatability from moment-to-moment, and even from day-to-day, of the ensemble average were considered and reported in Wilder (1992)

A basic premise of this work is that the wake of the oscillating airfoil is two-dimensional. Since it was not possible to measure directly the third velocity component with the equipment available, an indirect method was employed to confirm the two-dimensionality of the flow. Because a two-dimensional flow must be invariant in the third dimension (here the spanwise or z-direction), a comparison of the velocity components measured at several spanwise locations provides a sufficient measure of the two-dimensionality. Measurements were made in the upper row of vortices ($x/c_g = 2 \cdot 0$, $y/c_g = 0 \cdot 1$) and at five different z-locations across the water tunnel span. The measurements cover a span of 5 cm, or $0 \cdot 5 c_g$ (25% of the test-section span) and are centered about the tunnel center line. The ensemble-averaged velocity time records for the five locations are within the expected daily variation of the ensemble averages (Wilder 1992).

The use of finite differencing in estimating derivatives introduces errors into the calculated results. These errors depend on the measurement grid size and the degree of randomness of the data. An estimation of this error was determined by evaluating the sufficiency of the continuity equation on a grid element (Imaichi and Ohmi, 1983). The error for the grid element at (i, j) is

$$\varepsilon_{ij} = \left| \frac{(\partial u/\partial x)_{ij}\Delta x\Delta y + (\partial v/\partial y)_{ij}\Delta y\Delta x}{U_\infty \Delta y} \right|, \tag{8}$$

where the grid step sizes are Δx and Δy. The error is given as a percentage of the inflow to the grid cell ($U_\infty \Delta y$). Wilder (1992) indicates that the error is less than 1% of $U_\infty \Delta y$ for over 45% of the grid cells.

The errors introduced when second derivatives are calculated in terms of increased data were estimated to be much higher, namely the order of 5%. Such errors affect the caculation of pressure via equation (5). A more significant error in the calculation of pressure may be due to the fact that p_∞ in equation (6) is assumed to have a constant value. This pressure might vary with time due to upstream propagating disturbances. Moreover, it is found that the result of the integration was somewhat affected by the path of integration. As a result, the overall error was estimated to be up to 12% of the undisturbed free-stream value. However, spatial pressure variations, namely the location of peaks and valleys along the blade surface were consistent to within 1% of the chord length, regardless of the path of integration.

3. RESULTS AND DISCUSSION

The results are presented for steady velocity measurements around the target airfoil and unsteady measurements during the airfoil–vortex interaction. Three cases of unsteady results are presented: (i) a counterclockwise rotating vortex passing over the target airfoil at
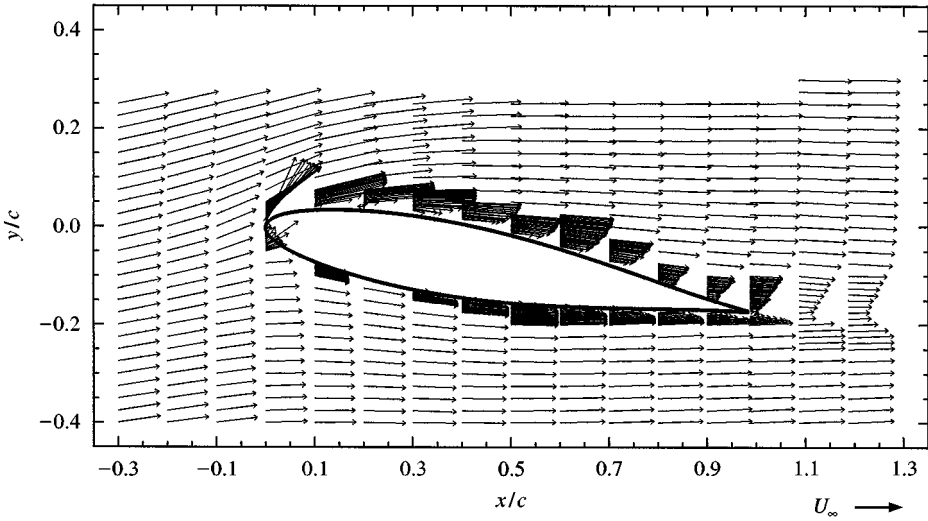
Figure 5. Steady velocity vectors around a NACA 63_2A015 at $\alpha = 10°$. Every seventh column of data is shown. The arrow beneath the frame is the scale of the magnitude of the velocity vectors.

a zero-degree angle of attack; (ii) a similar interaction with the airfoil at a $10°$ angle of attack, and (iii) a direct encounter (head-on collision) with the counterclockwise vortex (which includes a near miss below the airfoil with the clockwise vortex), $\alpha = 10°$. In the first two cases data are presented along tight two-dimensional grids. In the latter case, we employ the window method, discussed in Section 2, to determine the instantaneous vorticity fields. In each case, the reduced frequency and the reduced amplitude of the vortex generator were $k = \omega c_g/(2U_\infty) = 2.05$ and $\Delta\alpha = \pm 10°$, respectively, and the Reynolds number based on the target–airfoil chord length was very nearly Re $= 19\,000$ ($c = 15.24$ cm, $U_\infty = 12.5$ cm/s).

3.1. STEADY-STATE MEASUREMENTS

A complete mapping of the steady-state flow field around the blade model was obtained for the $10°$ angle-of-attack case. The vortex generator was removed from the tunnel for these measurements. Great care was taken to obtain data on a very tight grid. The velocity was measured on 112 columns in the domain,

$$- 0.3 \leq x/c \leq 1.2, \qquad - 0.4 \leq y/c \leq 0.25, \tag{9}$$

with, $\Delta x = 0.0125c = 1.905$ mm and $\Delta y = 0.025c = 3.81$ mm. A finer step size, $\Delta y = 0.0025c = 0.381$ mm was adopted close to the airfoil surface, in order to resolve the boundary layer. With this choice of the grid sizes, approximately 10 points were placed within the boundary layer in the first 20% of the airfoil and more than 20 in the aft region. The velocity measurements were averaged over 10 s to ensure a stable mean. Figure 5 is a vector plot of the steady velocities. For clarity, only every seventh column is shown.

One of the main goals of this effort is to provide a very carefully documented benchmark case for code validation. The steady case studied here is the first step in the analysis and data along a tight grid are necessary to allow careful comparisons with numerical results. These data are available on disk to anyone who would request them from the authors.
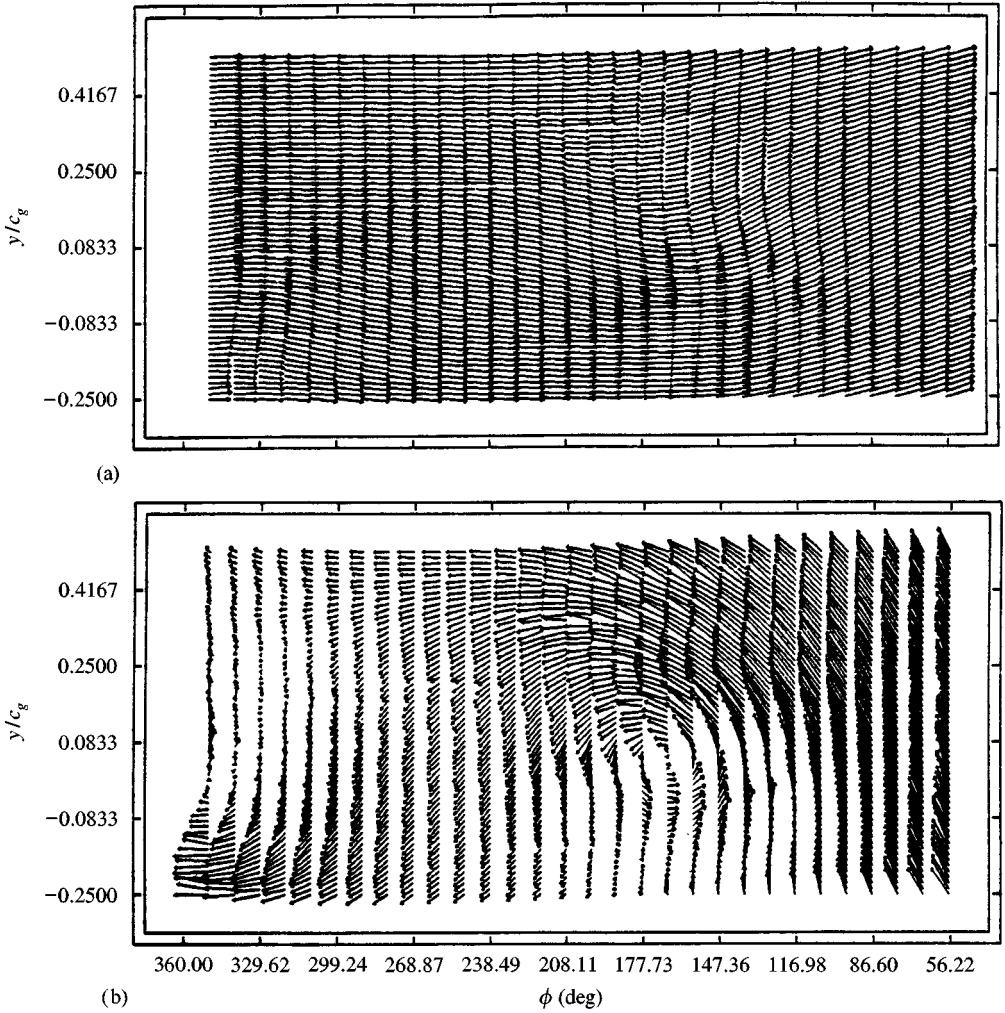
Figure 6. A 2-D velocity vector field constructed form a 1-D time record: (a) total velocity $\mathbf{V}$(b)$\mathbf{V} - U_d$.

The steady surface pressure distribution was determined from equation (5). The velocity was set to zero at the surface of the airfoil, and this value was used in a three-point, upwind, finite-difference formulation to determine the gradients at the boundary. The pressure gradients were integrated by repeated application of the trapezoidal rule. Pesce (1990) showed that higher-order integration schemes produced similar results. The calculated pressures agree quite well with theory, except on the first 20% of the upper surface. The pressure coefficients were integrated to find a lift coefficient of $C_l = 0.8$, which underestimates the ideal lift coefficient of $C_l = 1.07$. The lift can also be determined from the circulation about the airfoil. The circulation, evaluated with the data presented in Figure 5, is

$$\frac{\Gamma}{U_\infty c_g} = \oint \frac{\bar{V}}{U_\infty} \frac{\mathrm{d}l}{c_g} = 0.544, \tag{10}$$

and is clockwise around the airfoil. The ideal flow solution from conformal mapping is $\Gamma/(U_\infty c_g) = 0.5455$, which differs by less than 0.3% from the experimentally determined value.

This exercise indicates that even though velocity components were measured with great care and profiles appear to be very smooth, calculations of pressure distribution by evaluating terms in the Navier-Stokes equations introduce large errors in the immediate vicinity of the leading edge. A similar conclusion was arrived at by Mathioulakis and Telionis (1987, 1989). On the other hand, contour integration in terms of velocity measurements provides a much more reliable estimate of bound circulation and lift.

3.2. CONDITIONS FOR THE UNSTEADY MEASUREMETNS

The pitching airfoil sheds vorticity which quickly rolls up and forms coherent vortical structures (Wilder 1992; Wilder *et al.* 1996). Measurements were made in the wake of the pitching airfoil with the target airfoil removed. The velocity field in a fixed frame of reference indicates a wavy pattern as shown in Figure 6(a). This field was constructed by employing the Taylor hypothesis on the data obtained along a single vertical station. The vortical character of the field is better exposed if the velocity field is presented in a frame of reference moving with the vortices [Figure 6(b)]. An important finding of Wilder *et al.* (1996) is that the vortical structures thus generated contain a finite core of distributed vorticity much like the cores that trail the tip of a helicopter blade.

The wake of the pitching airfoil consists of vortices geometrically arranged in a way similar to a Kármán vortex street, i.e., the wake of a bluff body. However, for the present reduced frequency, the vortices have the opposite sense, that is the upper row is in the counter-clockwise sense and the lower row is in the clockwise sense. We define the first as positive and the second as negative. Moreover, the vortex street obtained here is relatively cleaner than the wake of a bluff body, i.e., contains much lower levels of turbulence in the space between vortices. Equal-sign vortices are spaced by a distance of $1.75c_g$ or $1.17c$.

The disturbing vortices were designed to match the characteristics of vortices normally encountered in the BVI problem. Two basic parameters control this process: the ratio of disturbing vortex to bound circulation Γ/Γ_b and the ratio of the disturbing vortex core diameter to the target blade cord, d/c. The vortex core diameter, d, is a measure of the extent of vorticity contained in a vortical structure. This is usually defined as the diameter of the ring where the vorticity magnitude is 10% of the core maximum. This ring will be referred to later as the "edge of the vortex." Hardin & Lamkin (1987b) indicate that in practice the ratio Γ/Γ_b is around 0.2. The value of this parameter in this investigation is 0.23. Straus *et al.* (1990) report $d/c = 0.1$, Srinivasan and McCroskey (1993) employed $d/c = 0.167$ in their calculation. This parameter has a value of 0.1 in the present experiments.

Measures of the vortex strength are Γ/Uc or Γ/v. Straus *et al.* (1990) report $\Gamma/Uc = 0.1$ and 0.15, and Srinivasan & McCroskey (1993) chose 0.133 and 0.177. Booth (1986, 1987a) achieved $\Gamma/Uc = 0.7$, while in the presnt experiments $\Gamma/Uc = 0.5$. Straus *et al.* (1990) report $\Gamma/v = 12\,795$, Gursul & Rockwell (1990) measured $\Gamma/v = 2\,200$, and in the present experiments $\Gamma/v = 6\,300$.

In the rest of this section we describe the conditions and provide numerical values of the parameters for the three basic experiments.

3.2.1. *Case (i); Target airfoil at $\alpha = 0°$: close encounter*

The target airfoil was aligned to interact with the upper row of vortices (the counterclockwise rotating vortices) in the wake of the oscillating airfoil. This was achieved by displacing the airfoil above the symmetry line of the wake by a vertical distance of $\Delta h = 0.09c$. Even though the nose of the airfoil was above the linear extrapolation of the path of the vortex, the trajectories of the vortices were deflected above the airfoil surface. This is because the
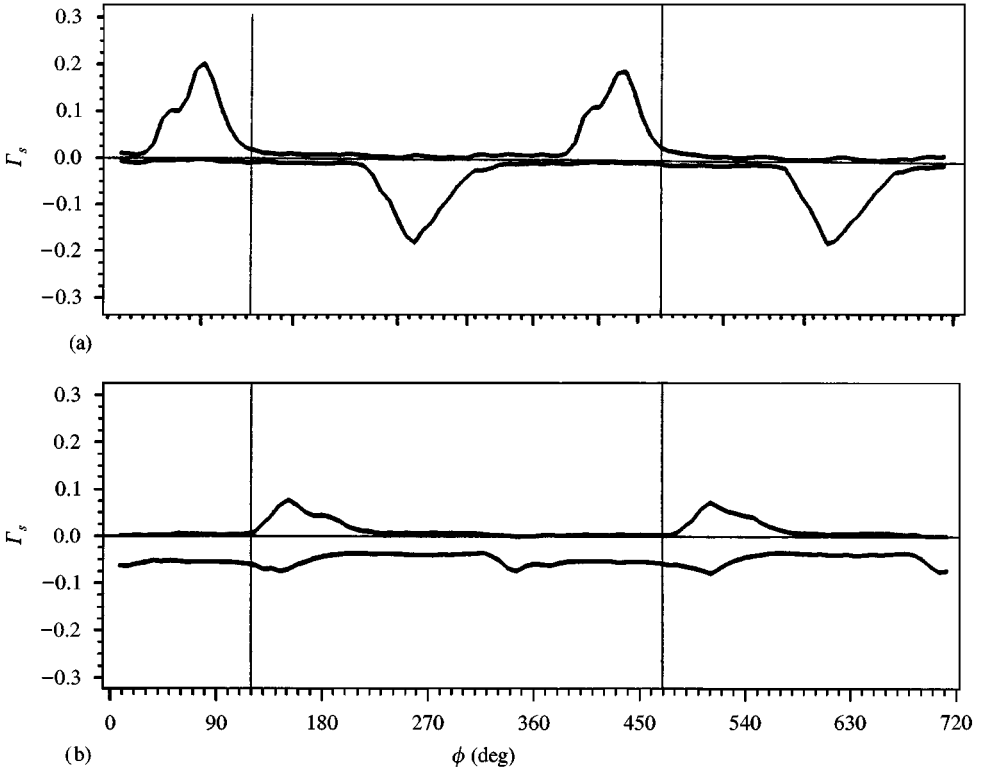
Figure 7. Sectional circulation along (a) at $x = -0.2c$, (b) at $x = 0.15c$.
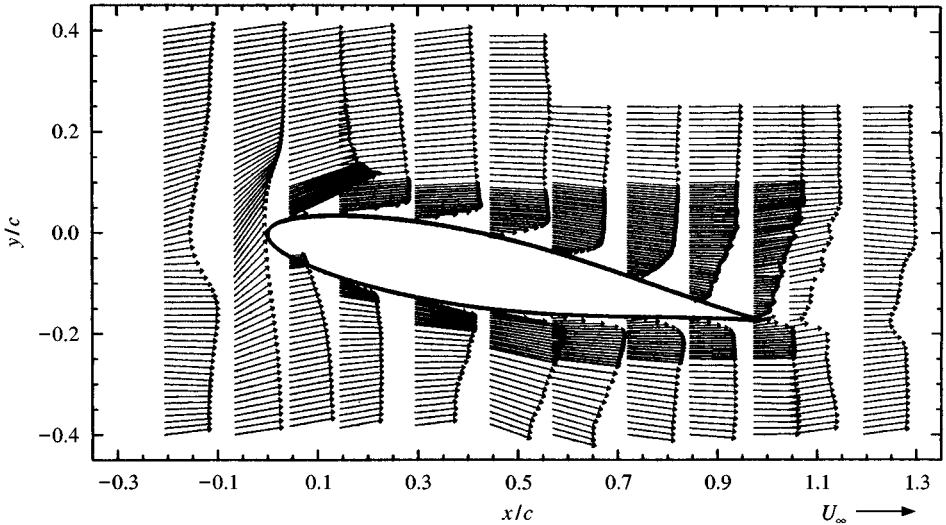

Figure 8. Instantaneous velocity vector field, $\alpha = 10°$, $\phi = 81°$ (direct encounter).

approaching vortex induces circulation to the blade and this in turn deflects the trajectory of the approaching vortex upward. The choice of Δh is therefore a painstaking process to achieve the desired interaction. Ensemble-averaged velocities were obtained along 27 survey lines from $x/c = -0.3$ to 0.35 in increments of $\Delta x/c = 0.025$, at 41 points per column from $y/c = -0.2$ to 0.3 in increments of $\Delta y/c = 0.0125$, and at 50 time instances per

period of oscillation with $\Delta t = 0.0248$ s. Ensemble-averaged velocities were recorded for two complete oscillations of the vortex generator, the two separate cycles being used to assess the repeatability of the process. In this case, no measurements were made beneath the airfoil ($x/c \geq 0$, $y/c \leq 0$), and at several stations near the leading edge measurements were impossible, because one of the laser beams was blocked by the airfoil. Twenty to thirty time records were obtained in each ensemble average and thirty in the boundary layer regions where the velocity magnitude and therefore, the data rates were lower.

Instantaneous vorticity and circulation were later calculated in terms of these data. In Figure 7, the sectional circulation is shown at a station $0.2\,c$ upstream of the airfoil leading edge, and at a station $0.15\,c$ downstream of the leading edge. Recall that according to definition (4), this quantity catches the amount of vorticity that crosses the section at a certain instant. Here positive and negative sectional circulations are collected separately. It is therefore possible to track the passage of the oncoming disturbing vortices but secondary vortices, i.e. vortices generated due to blade-vortex interaction, are lumped with the sectional circulation of the opposite sign. Recall that according to definition (4), this quantity catches the amount of vorticity that crosses the section at a certain instant. The figure clearly illustrates the repeatability of the interaction. At the upstream location $x = -0.2\,c$, we see the passage of the primary positive and negative vortices in the street. At the next position $x = -0.15\,c$, the positive circulation curve represents the positive primary vortices passing over the blade surface. The data for this case were obtained only above the airfoil and therefore the negative primary vortex does not appear. Associated with the primary positive vortices is a secondary concentration of negative vorticity induced at the airfoil surface by the primary vortex. A small piece of the negative primary vortex also passes over the airfoil, and is the source of the peak in negative circulation seen $180°$ ahead of the positive circulation.

3.2.2. *Case (ii) Target airfoil at* $\alpha = 10°$: *close encounter*

The target airfoil was displaced further from the wake symmetry line for this case by ($\Delta h = 0.1c$), but again, the vortex core passed above the airfoil surface. At incidence, the airfoil had a greater influence upon the vortex trajectory. Measurements were made on two more survey lines, extending the grid to $x/c = 0.4$, and the range of the columns was shifted to include more of the region above the airfoil: $y/c = -0.15$ to 0.35. The time resolution was doubled, $\Delta t = 0.0124$ s, and only one cycle was saved.

3.2.3. *Case (iii); Target airfoil at* $\alpha = 10°$: *collision*

One of the goals in this research was to study the direct encounter of the vortex and airfoil. But the interaction is a nonlinear process, so that small adjustments in position to achieve direct encounter of the target airfoil sometimes yielded disproportionate changes in the vortex trajectories. Adjusting the airfoil position required a lengthy and tedious procedure. In order to facilitate the alignment process, velocity measurements were made along only two survey lines, separated by a small distance and located just upstream of the airfoil nose. At this stage, the window method described in Section 2.2 was first applied to airfoil–vortex interaction measurements. Vorticity, as a function of time, was calculated along the column and vorticity fields were constructed by assuming that, over short distances, the vorticity propagates with the local velocity. Determining the location of the vortex from so few measurements greatly accelerated the alignment process. Moreover, this preliminary study indicated that the window method could be used to study the interaction.

With the airfoil positioned for a direct encounter, a complete series of measurements were made. Each window measurement consisted of a pair of survey lines separated by the
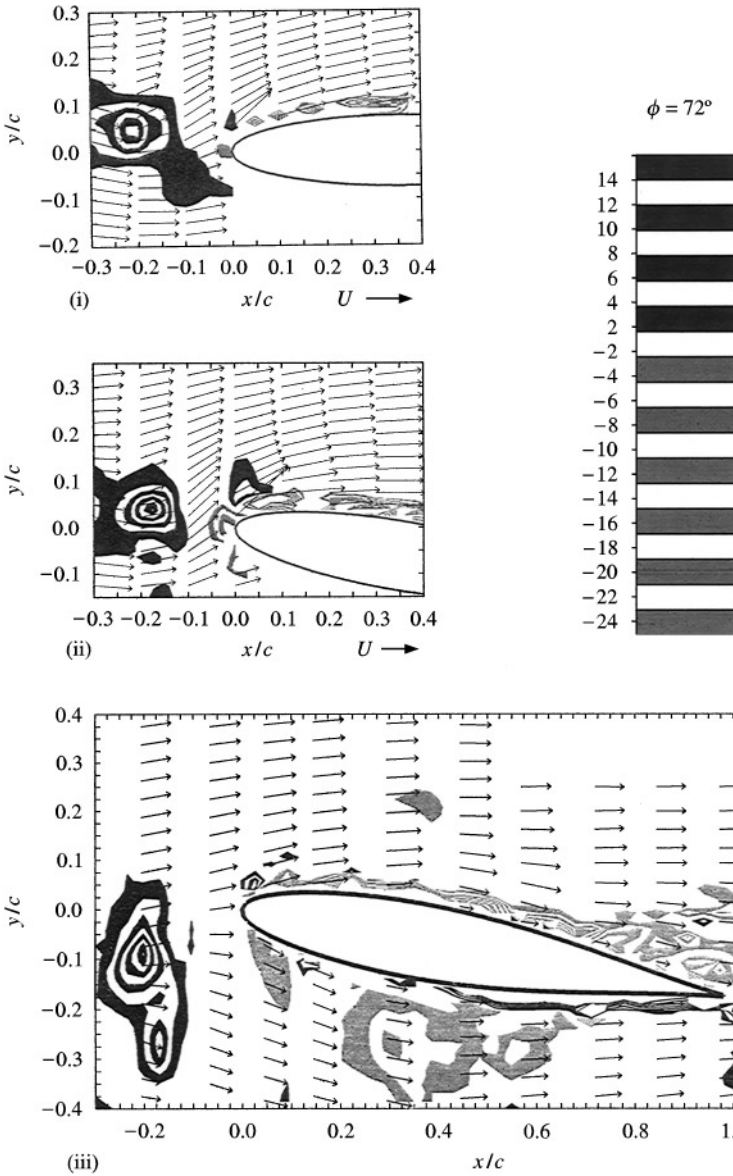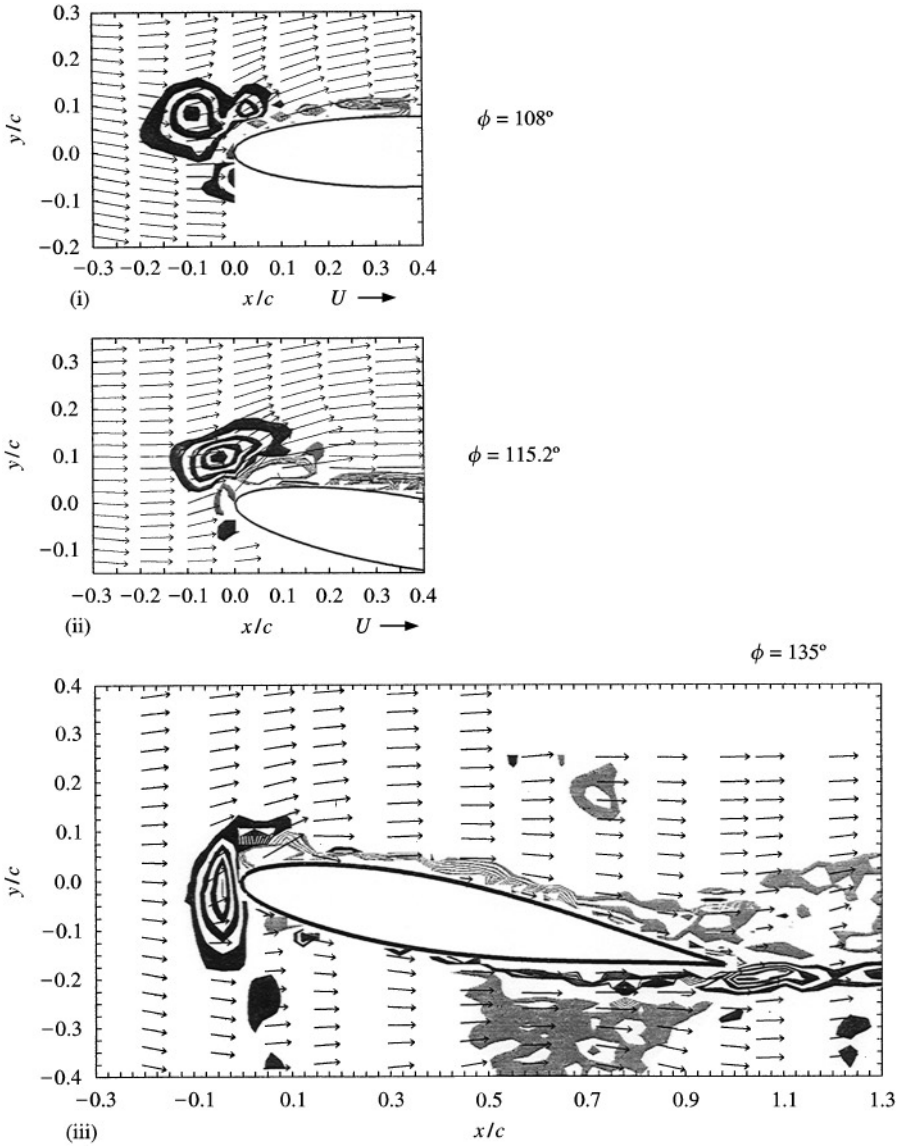
Figure 10(a). Vorticity contour maps: (i) $\alpha = 0°$, $\Delta h = 0.09c$; (ii) $\alpha = 10°$, $\Delta h = 0.1c$; (iii) $\alpha = 10°$, $\Delta h = 0.125c$.

distance $\Delta x/c = 0.0125$. The survey lines covered the range $-0.4 \leq y/c \leq 0.4$, with a step size of $\Delta y/c = 0.005$ in the boundary region of the target airfoil and $\Delta y/c = 0.0125$ elsewhere. The windows were centered at

$$x/c = -0.20, \quad -0.06, \quad 0.05, \quad 0.15, \quad 0.30, \quad 0.45, \quad 0.575, \quad 0.725, \quad 0.85, \quad 0.978,$$
$$1.05, \quad 1.20.$$

The time resolution was doubled over the previous case, giving $\Delta t = 0.0062$ s, and measurements were recorded for 200 instances over the period of the vortex generator ($T = 1.24$ s). A complete sequence of the velocity and vorticity fields can be found in Wilder (1992). A representative velocity vector field is given in Figure 8. This figure is a
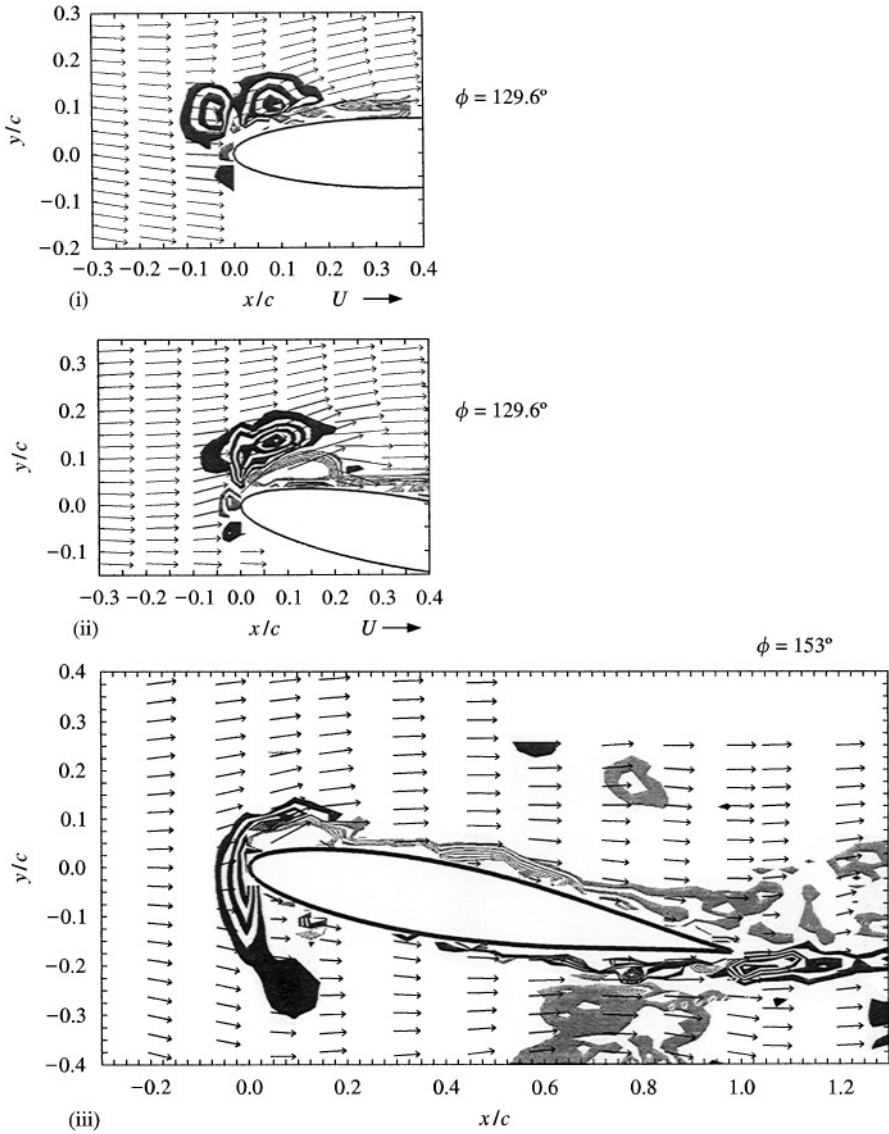
Figure 10(b). Vorticity contour maps: (i) $\alpha = 0°$, $\Delta h = 0.09c$; (ii) $\alpha = 10°$, $\Delta h = 0.1c$; (iii) $\alpha = 10°$, $\Delta h = 0.125c$.

representative snapshot of temporally developing fields. It contains a true representation of the velocity data obtained on all points of the measuring grid. In subsequent figures we add vorticity distributions but to preserve the clarity of the figures, we present velocity data only on a few selected grid points. Moreover, we present frames of data that capture the temporal evolution of the phenomena under consideration. The frame of reference of the velocity vectors is attached to the fixed target airfoil.

3.3. RESULTS FOR THE UNSTEADY MEASUREMENTS

In Figure 9, the velocity vectors are presented in terms of small arrows. The lengths of these arrows are proportional to the local velocity magnitude and therefore, because of the
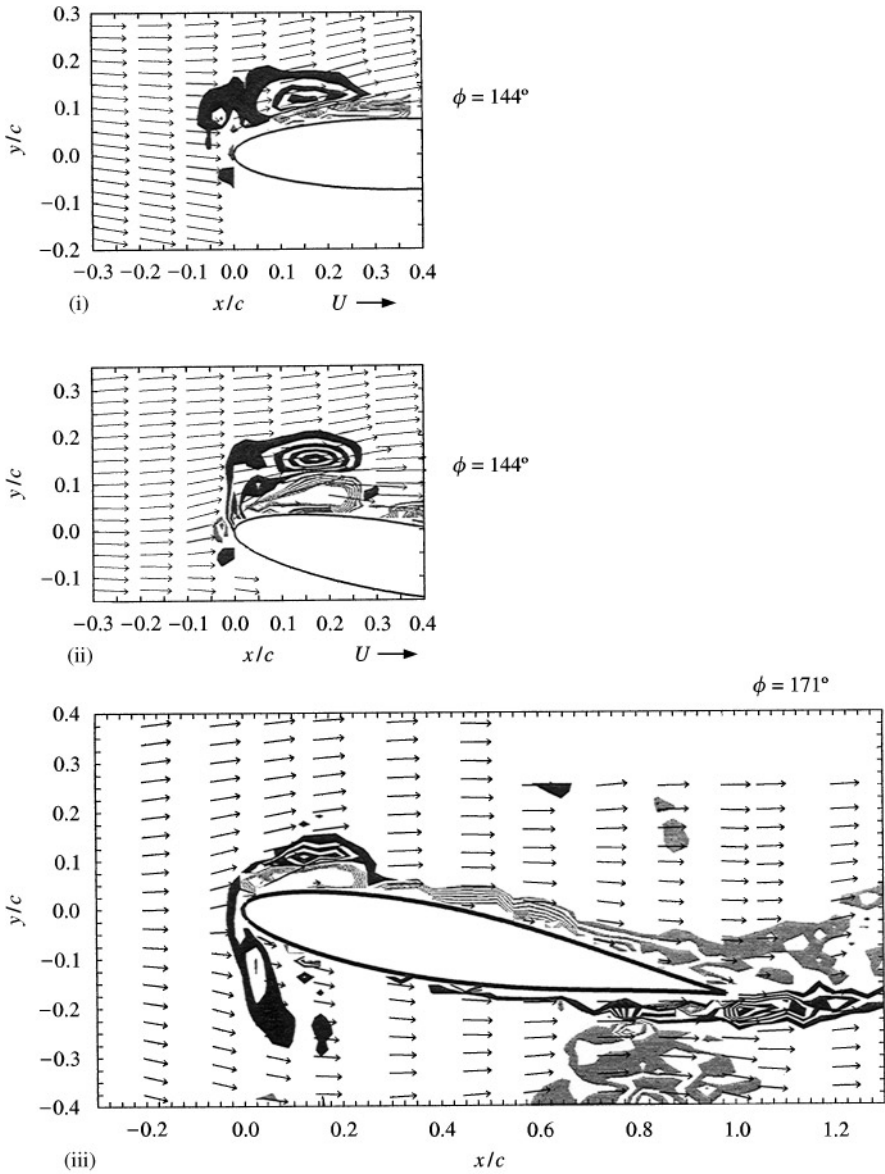
Figure 10(c). Vorticity contour maps: (i) $\alpha = 0°$, $\Delta h = 0.09c$; (ii) $\alpha = 10°$, $\Delta h = 0.1c$; (iii) $\alpha = 10°$, $\Delta h = 0.125c$.

limitation of the figure size, these figures make a poor presentation of the quantitative information obtained. This information, including data on all intermediate phases is available on a disk.

The approaching vortical structure appears to be very nearly circular in shape. Its vorticity is distributed over a core equal to about 20% of the target blade chordlength. The vortices periodically induce a locally high apparent angle of attack. In the leading edge region of the airfoil, the flow is similar to that of an airfoil oscillating in pitch. The stream periodically exceeds the static stall angle of approximately 14°, and the flow exhibits some features of dynamic stall. Since the high flow angles are localized to the neighborhood of the vortices, stall has a limited extent as well. As the positive vortex approaches the airfoil, the flow separates and creates a separation bubble which grows until it covers approximately
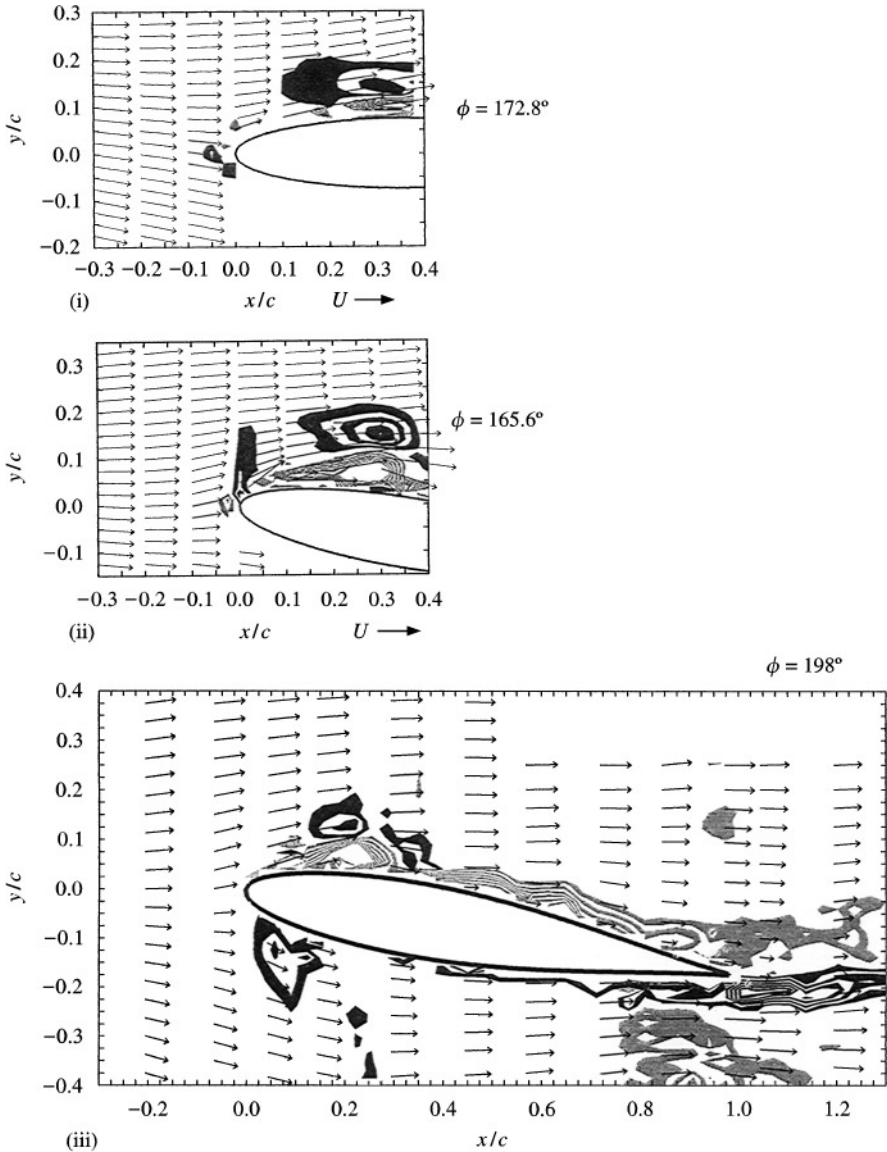
Figure 10(d). Vorticity contour maps: (i) $\alpha = 0°$, $\Delta h = 0.09c$; (ii) $\alpha = 10°$, $\Delta h = 0.1c$; (iii) $\alpha = 10°$, $\Delta h = 0.125c$.

20% of the leading edge. Negative vorticity accumulates in the bubble until it essentially forms a secondary vortex, reminiscent of the unsteady stall vortex. The disturbing and stall vortex subsequently start drifting as a pair over the suction side of the blade.

Vorticity fields for each of the three interaction cases are compared with one another in Figure 10. The bands are contour levels of nondimensional vorticity, $\Omega c_g/U_\infty$, shown in alternating black/grey and white, each band corresponding to two units of vorticity, and the lowest band beginning with a magnitude of $\Omega c_g/U_\infty = 2$. Positive vorticity (counterclockwise rotation) is denoted by black contour bands, and negative vorticity by gray bands. To preserve the clarity of the figure, only a few of the available velocity vectors are included in these frames.

Figure 10(e). Vorticity contour maps: (i) $\alpha = 0°$, $\Delta h = 0.09c$; (ii) $\alpha = 10°$, $\Delta h = 0.1c$; (iii) $\alpha = 10°$, $\Delta h = 0.125c$.

Vorticity contours illustrate the displacement and distortion of the vortices. For each of the three cases, the primary positive vortex is shown at the same x/c location in the first frame. In other words, each sequence is started with the disturbing vortex approximately 0·3 chords upstream of the blade nose. Notice that as the vortex moves downstream, the events in the three cases go out of phase with one another. The mutually induced velocity between airfoil and vortex is highly dependent not only on the angle of attack of the airfoil, but also on the closeness of approach of the vortex. We observe that for the Case (i), even though the vortex approaches the blade at the same elevation as in Case (ii), there is no stall bubble generated. This explains the fact observed in practice that blade–vortex interaction with unloaded blades, i.e., $\alpha = 0°$, produces very low load fluctuations and generates minimal noise.
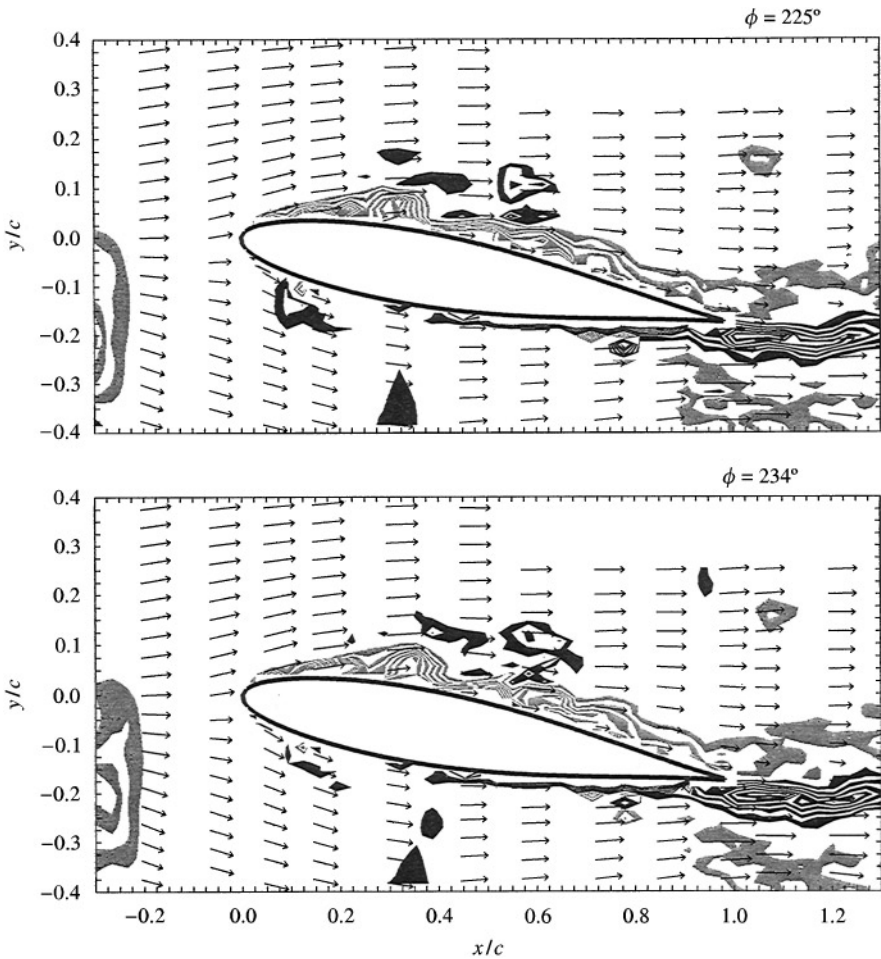
Figure 10(f). Vorticity contour maps: Case (iii) only; $\alpha = 10°$, $\Delta h = 0.125c$.

Equally interesting is the case of direct encounter of the vortex with the leading edge, i.e., Case (iii) in Figure 10. In this case, the oncoming vortical structure is split in two. The upper structure propagates over the upper surface of the blade and induces a secondary vortex just as in Case (ii). The lower structure propagates with a slower velocity and stretches vertically, i.e., away from the blade. Intriguing here is the behavior depicted in the range of phase $\phi = 198–234°$. In these frames, we observe that first, the disturbing vortex and then the stall vortex break in half and later disintegrate to many smaller structures. This explains the fact that the detrimental effects of blade–vortex interaction, i.e., dynamic loads and acoustic disturbances have their sources near the leading edge (Rockwell 1984; Booth 1986, 1987; Booth & Yu, 1986). Apparently, for the case of direct interaction, large vortical structures retain their identity in the first 20–40% of the chord but soon after break up into smaller structures. But for a vortex skimming over a loaded airfoil [Case (ii)], disturbing and induced vortices retain their identity.

We calculated the trajectories of vortical structures over the airfoil for the three cases discussed here. These calculations were based on numerical estimates of the center of gravity of the vorticity distribution. At each phase, the centroids for all positive and negative vorticity satisfying a condition of vortical identity were calculated. The trajectories of the
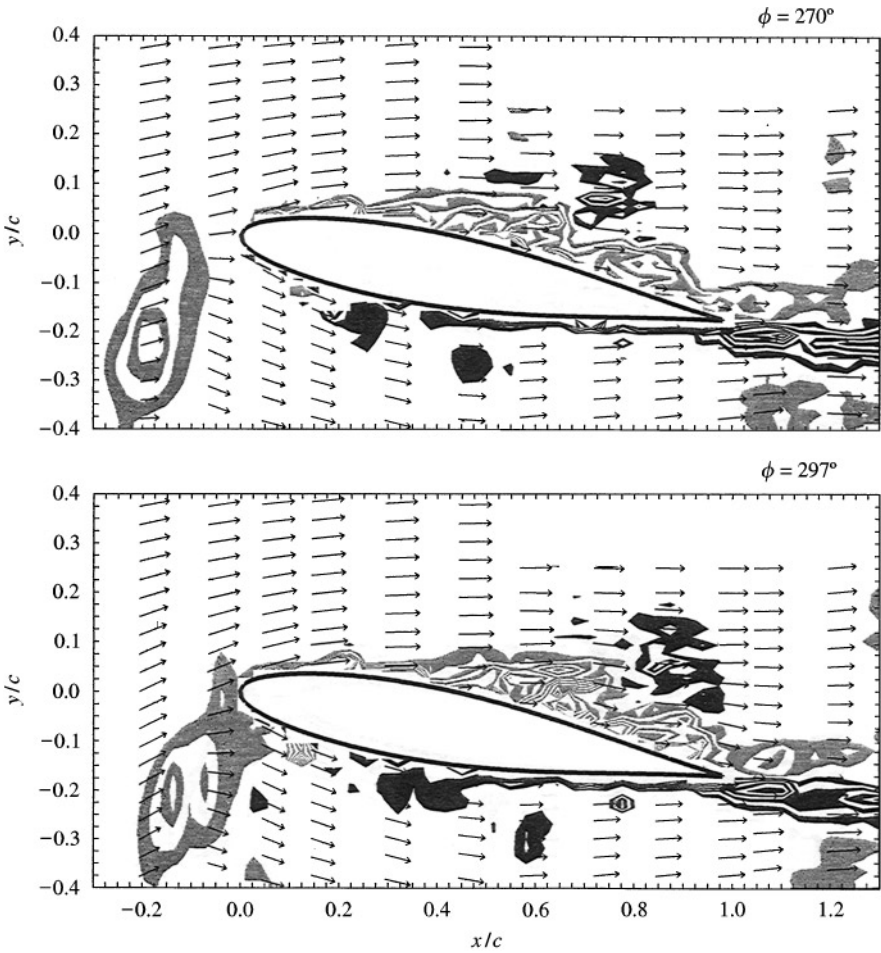
Figure 10(g). Vorticity contour maps: Case (iii) only; $\alpha = 10°$, $\Delta h = 0.125c$.

primary and secondary vortices are presented in Figure 11. The symbols indicate the location of vortex cores which were determined by finding the center of gravity of single-sign vorticity.

The circulation of the primary vortex and of the secondary vorticity induced on the airfoil was calculated at each measured time instant, and the results are presented in Figure 12. This is essentially a temporal history of the strength of the vortices. The circulation was determined by a surface integral, i.e., by summing the vorticity over the region associated with an entity under consideration

$$\Gamma_s = \sum_{i,j} \Omega_{i,j} \Delta x \Delta y, \tag{11}$$

where Ω_{ij} is the vorticity at the node i, j and Δx and Δy are the step sizes used in the finite-difference calculations of the vorticity. With the airfoil at $\alpha = 0°$, the strength of the vortex decreased by 30% of its upstream value while passing along the airfoil surface. The vorticity around the blade varied little throughout the encounter, increasing a little absolutely (8% of the upstream circulation of the positive primary vortex). This is the negative vorticity contained in the attached boundary layer as well as the negative vorticity induced by the oncoming vortex. At all times, the blade circulation was less than half the
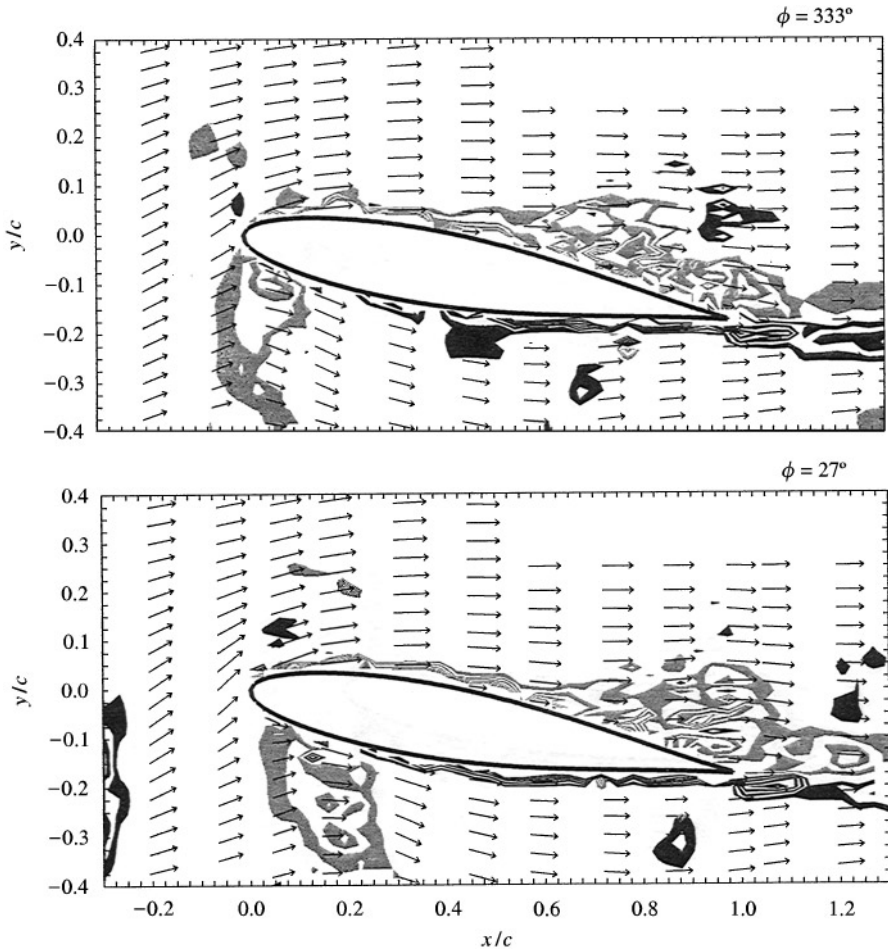
Figure 10(h). Vorticity contour maps: Case (iii) only; $\alpha = 10°$, $\Delta h = 0.125c$.

strength of the primary vortex. We see from the vortex trajectory (Figure 9) that the vortex is in close proximity to the airfoil surface. Friction between the fluid and the surface of the blade may be slowing down the vortical motion of the flow, resulting in a net decrease in the total circulation of the vortex.

This statement should not be misinterpreted. In two dimensions and away from solid surfaces, vorticity is conserved. Viscosity only facilities diffusion, but diffusion could bring vorticity in the proximity of solid surfaces which act as vortex sources or sinks depending on the sign of the pressure gradient.

The disturbing vortex had a considerably stronger influence on bound vorticity when the airfoil was at an angle of attack. With the vortex still 0·2 chord lengths upstream of the airfoil at $\alpha = 10°$, the circulation in the boundary layer was equivalent in magnitude to that of the vortex. This circulation grew absolutely by 23% during the approach of the vortex and another 19% as the vortex drifted over the airfoil and up to $x/c = 0.25$ ($\phi = 158.4°$). This growing circulation includes the secondary vorticity generated at the airfoil's leading edge. Unlike the $\alpha = 0°$ case, the primary vortex suffered a little during this encounter; only a 9% decrease in circulation was observed. Apparently, the strong secondary vorticity isolated the primary vortex from the airfoil surface and the frictional decreases experienced in the $\alpha = 0°$ case. The secondary and primary vortices were arranged such that a jet-like
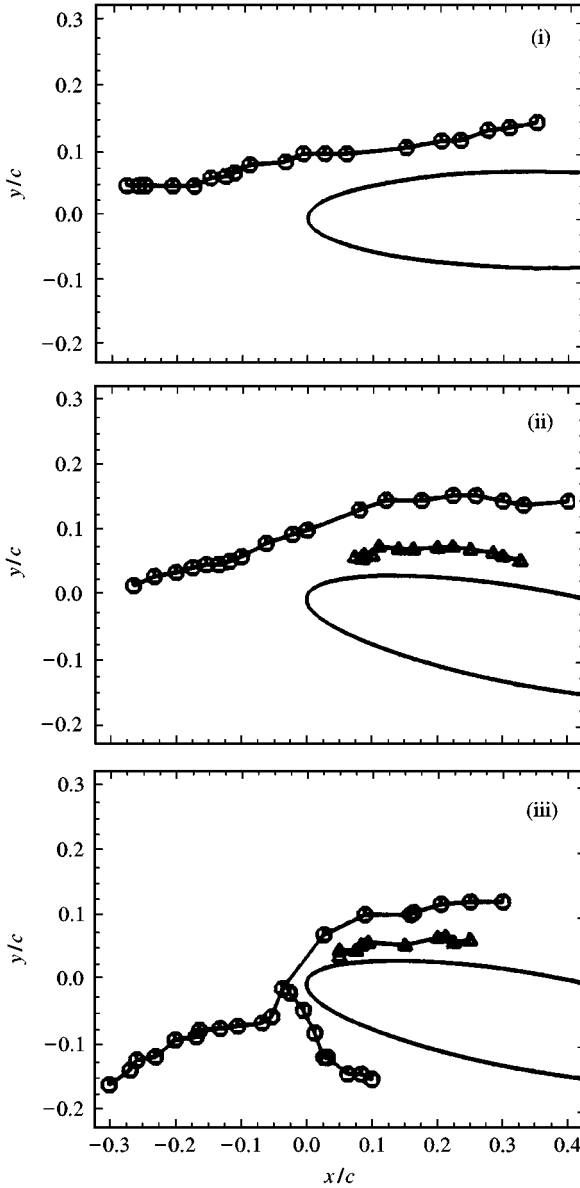
Figure 11. Trajectory of primary and secondary vortices for each case; (i) $\alpha = 0°$, $\Delta h = 0.09c$; (ii) $\alpha = 10°$, $\Delta h = 0.1c$; (iii) $\alpha = 10°$, $\Delta h = 0.125c$. $\bigcirc$, CCW vortex; $\triangle$, CW vortex.

flow, in the streamwise direction was produced between them (observable in the velocity vector profiles of Figure 9 and 10).

In the head-on collision case, the primary vortex was cut in two and the circulation of each piece was only a fraction of the upstream vortex strength. It was not possible to track each of these structures and estimate their total circulation.

3.4. THE SEVERITY OF BVI AND POSSIBLE ALLEVIATION

Figure 13 depicts the nondimensional sectional circulation as a function of time at several locations x/c in the flow. Recall that Γ_s is calculated by integrating along a vertical strip
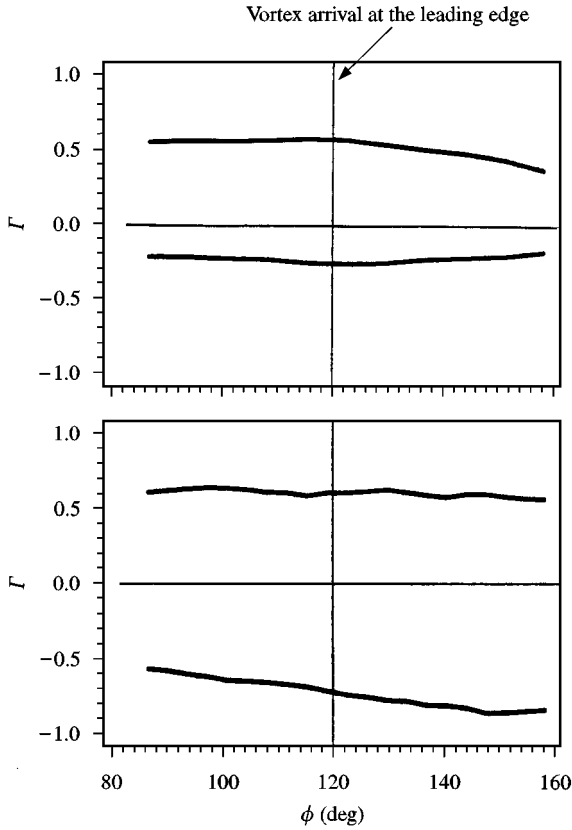
Figure 12. Variation of a primary and secondary circulation during the interaction: (a) $\alpha = 0°$, $\Delta h = 0.09c$, (b) $\alpha = 10°$, $\Delta h = 0.1c$.

containing two vertical measuring grid lines. The positive and negative contributions are collected separately. One can thus observe the passage of the two oncoming vortices as well as the generation of secondary vortices. The vertical reference lines in Figure 13(b) and beyond indicate the phase within the period at which the disturbing vortex reaches the leading edge and the phase at which the vortex core passes that particular location, x/c. The circulation associated with primary vortices is designated as Pp and Pn for the positive and negative vortices, respectively, and Sn designates the secondary negative vorticity (the stall vortex).

With the exception of Case (i) ($\alpha = 0$), we see evidence that at $x/c = 0.05$, a stall vortex begins forming at the leading edge, when the primary positive vortex is still more than 0.2 chord lengths upstream ($\Delta\phi = 45°$), and the primary negative vortex is beneath the airfoil at approximately $x/c = 0.35$. There is a growing bulge in the negative vorticity at the leading edge which extends over nearly 20% of the chord. At this x/c location, we see that the negative circulation begins to grow at $\phi \approx 45°$. At successive x/c stations, the primary and secondary circulations have similar temporal extents and peak at approximately the same phase, indicating that the two vortices move together, a fact that has also been observed in Figure 9.

It is observed that only for the loaded blade encountering a near miss with the oncoming disturbing vortex, the strength of the vortices is retained over the airfoil. In fact, in this case, the induced secondary vortex increases in strength beyond the magnitude of the disturbing vortex.

Care must be taken in interpreting the vorticity contour plots of Figure 10. Consider for example, Case (ii). As the primary vortex passes over the leading edge, it accelerates and is
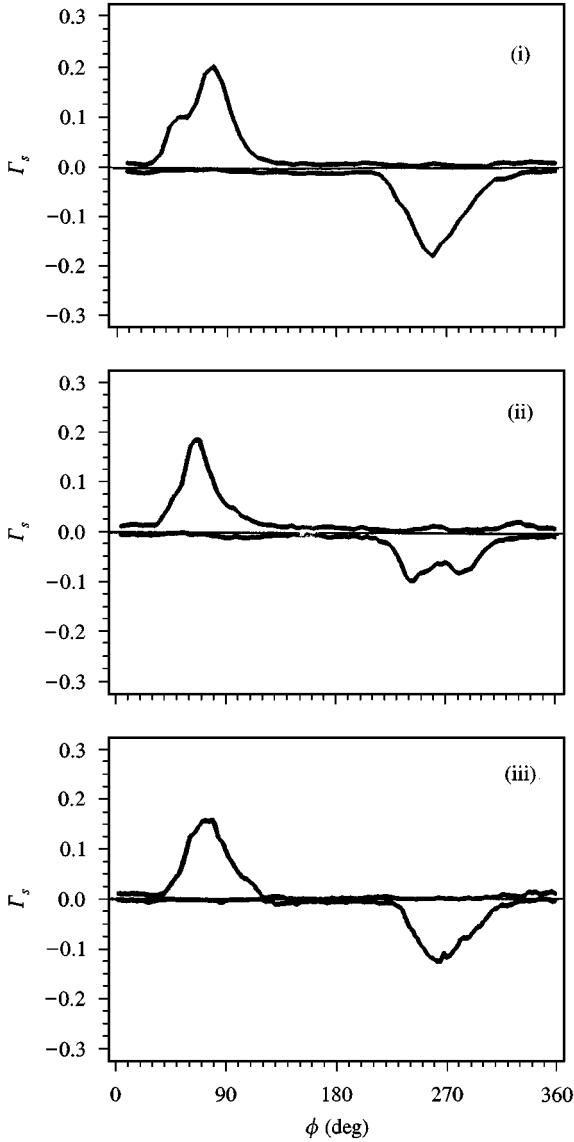
Figure 13(a). Sectional circulation flux for $x/c = -0.2$: (i) $\alpha = 0°$, $\Delta h = 0.09c$; (ii) $\alpha = 10°$, $\Delta h = 0.1c$; (iii) $\alpha = 10°$, $\Delta h = 0.125c$.

elongated into an oval shape. The elongation has the effect of locally decreasing the magnitude of vorticity, since vorticity is spread out over a larger area. Comparing the circulation flux at $x/c = -0.2$ and at $x/c = 0.06$, there is a 30% decrease in the maximum circulation while both peaks have the same width ($\Delta\phi \approx 90°$). This gives the impression that the strength of the vortex has decreased by 30% while traveling between these two stations, when in reality, at the second station a more diffuse vortex is passing by at a higher speed than at the first station. This is confirmed by evaluating the total circulation of the vortex at any particular phase, as shown clearly in Figure 13.

Unsteady surface pressure coefficients were calculated in terms of the measured velocities via equations (5). The variation of C_p at $x/c = 0.05$, 0.15 and 0.3 is displayed in Figure 14.
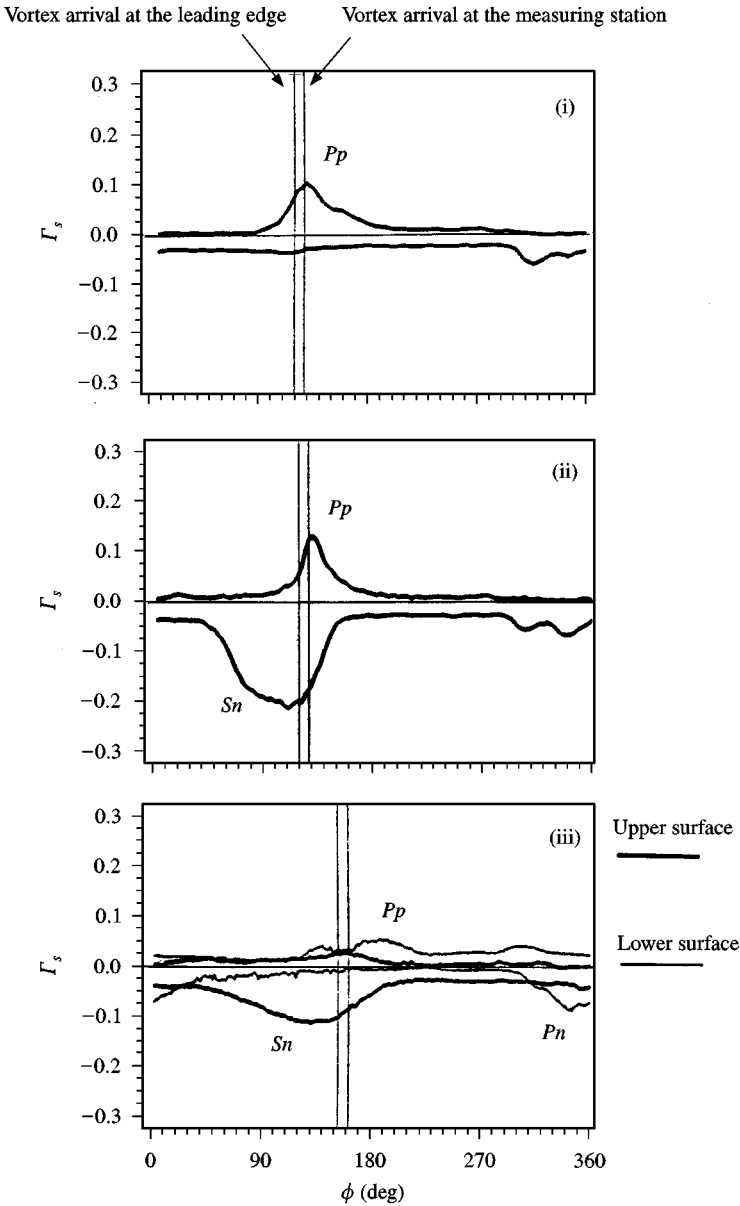
Figure 13(b). Sectional circulation flux for $x/c = 0.05$; (i) $\alpha = 0°$, $\Delta h = 0.09c$; (ii) $\alpha = 10°$, $\Delta h = 0.1c$; (iii) $\alpha = 10°$, $\Delta h = 0.125c$.

Vertical reference lines indicate again the phase at which the vortex core passed the leading edge and the measurement station in question, respectively. Horizontal reference lines represent the corresponding steady pressure coefficients for the upper and lower airfoil surfaces. For the $\alpha = 0°$ case, the corresponding steady-state flow values were taken from Abbott & von Doenhoff (1959). For the $\alpha = 10°$ cases, calculated steady pressure coefficients (Wilder 1992) in terms of the experimental data are indicated.

In all three cases, the pressure at $x/c = 0.05$ increased as the vortex approached and achieved a maximum as the *edge* of the vortex reached the leading edge. This occurred at
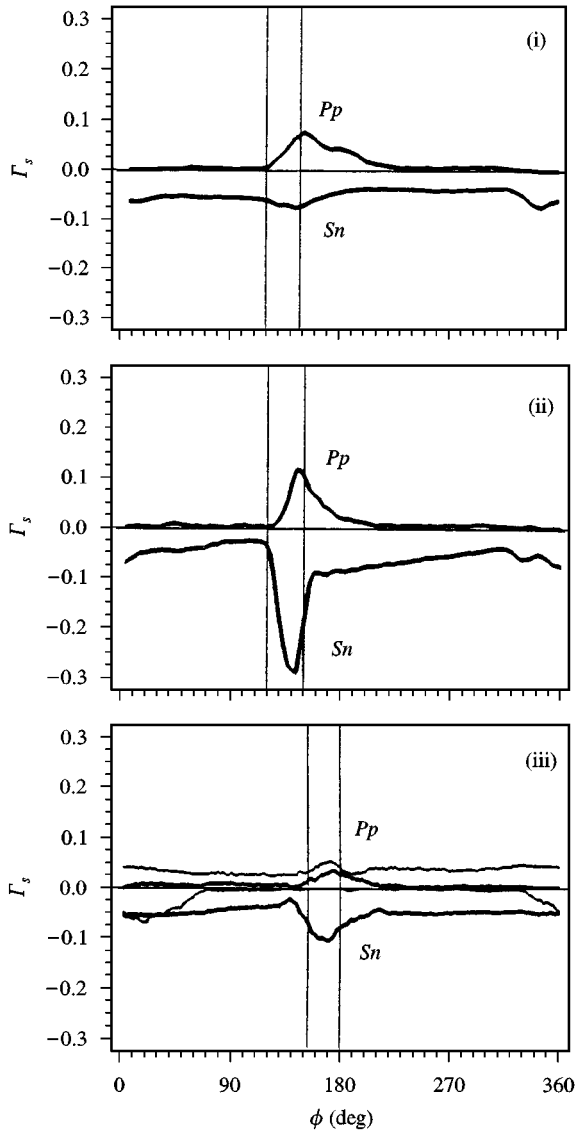
Figure 13(c). Sectional circulation flux for $x/c = 0.15$: (i) $\alpha = 0°$, $\Delta h = 0.09c$; (ii) $\alpha = 10°$, $\Delta h = 0.1c$, (iii) $\alpha = 10°$, $\Delta h = 0.125c$.

a phase of 90° for Cases (i) and (ii), but not until $\phi \approx 130°$ in the head-on collision case. By the time the vortex core passed the leading edge [$\phi \approx 120°$ for Cases (i) and (ii)] the pressure had reached a minimum. This minimum pressure did not occur in Case (iii) where the vortex is split, indicating that the minimum pressure may depend on the strength of the vortex. A second maximum value, which occurred around a phase of 130° in the first two cases, can be associated with vortex core moving beyond $x/c = 0.05$. After the vortex has moved beyond $x/c = 0.3$, the pressure settled down to a relatively constant value. This value was very near the steady value of pressure for Cases (i) and (ii), but lower for case (iii).

At the next two stations, $x/c = 0.15$ and 0.3, Case (ii) more closely resembles Case (iii) than Case (i) (the other close-encounter case). The peak in the pressure time record of Cases
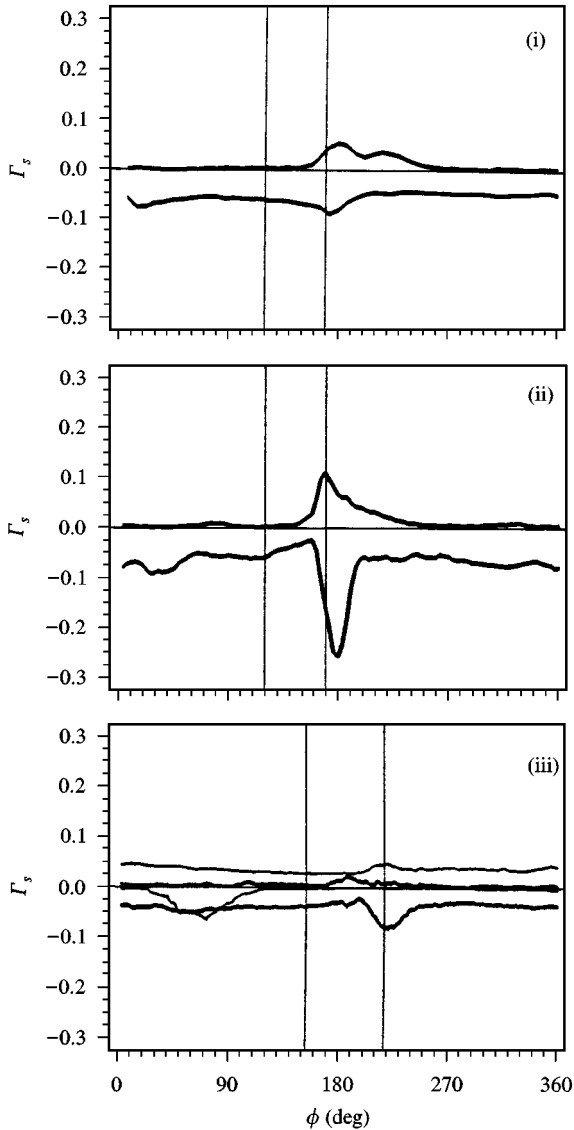
Figure 13(d). Sectional circulation flux for $x/c = 0.3$: (i) $\alpha = 0°$, $\Delta h = 0.09c$; (ii) $\alpha = 10°$, $\Delta h = 0.1c$; (iii) $\alpha = 10°$, $\Delta h = 0.125c$.

(ii) and (iii) is associated with the edge of the primary/secondary vortex pair arriving at each station. The pressure becomes steady after the vortices have passed. This indicates that the effects at the leading edge are strongly influenced by the closeness of the encounter, while the effects felt along the airfoil length are influenced more by the airfoil angle of attack [no secondary vortex formed in Case (i), the $\alpha = 0°$ case]. This again confirms the fact that the airfoil-vortex interaction is a leading edge phenomenon (Booth 1986; Rockwell 1984). A positive spike in the lower surface pressures of Case (iii) was observed at all stations along the airfoil chord at a phase of 60°. This spike does not move and cannot be associated with any structure visible in the vorticity contour maps.

The most important conclusion we can draw from Figure 14 is also the most striking new piece of information that this figure displays. The pressure oscillations with the largest
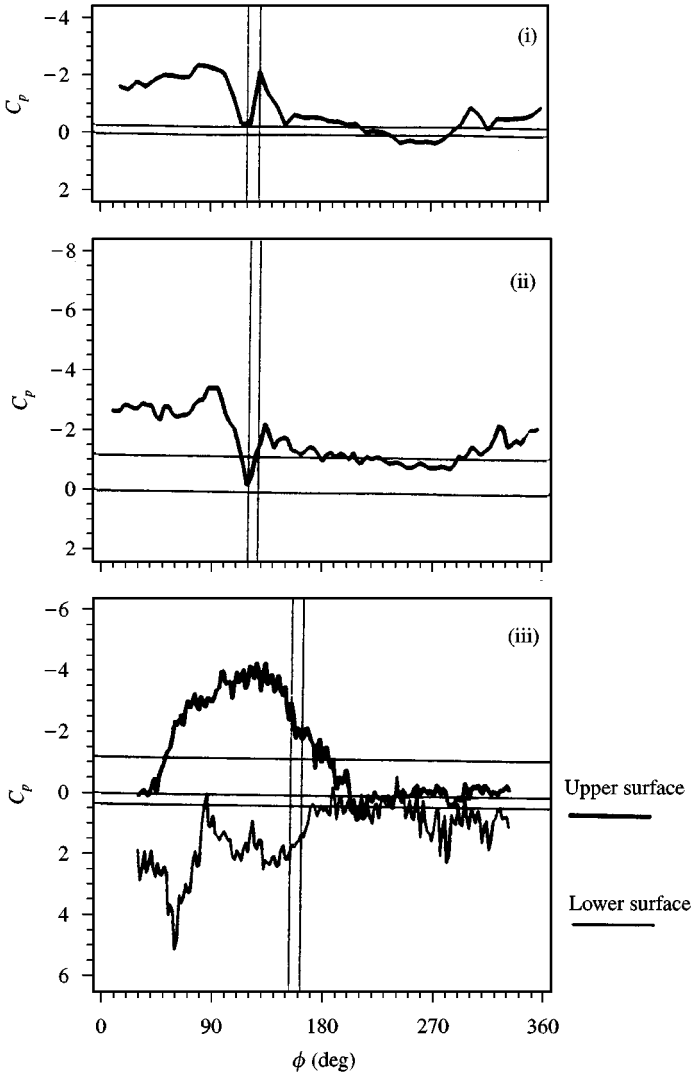
Figure 14(a). Surface pressure coefficients versus phase for $x/c = 0.05$: (i) $\alpha = 0°$, $\Delta h = 0.09c$; (ii) $\alpha = 10°$, $\Delta h = 0.1c$; (iii) $\alpha = 10°$, $\Delta h = 0.125c$.

amplitude are observed for the case of a loaded blade and a vortex which skims over its surface [Case (ii)]. Apparently, a vortex skimming over an unloaded blade [Case (i)] quickly loses its strength, whereas a vortex colliding with the leading edge breaks up into smaller structures and in both of these cases, i.e., Cases (i) and (iii) in Figure 14, the pressure signature is void of organized oscillations with large amplitude.

Hardin & Lamkin (1987a) developed a very simple inviscid theory of BVI by modeling the disturbing and the bound vortical structures by two ideal vortices. They predicted that the noise level is proportional to the product of the circulations of the disturbing and the bound vortex. Therefore, a disturbing vortex will generate more sound if it interacts with a loaded blade which carries bound vorticity, than with an unloaded blade. The fact that the pressure amplitudes we found over the unloaded blade are lower than the amplitudes in the loaded blade confirm this prediction. Moreover, a further reduction in the noise beyond
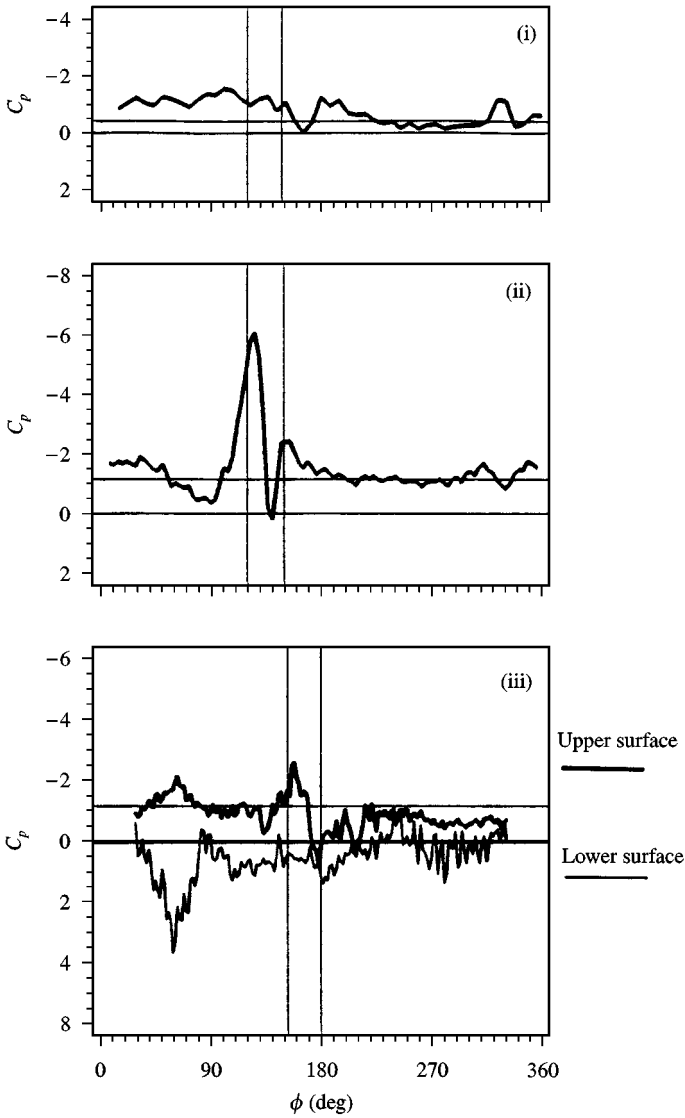
Figure 14(b). Surface pressure coefficients versus phase for $x/c = 0.15$.

the Hardin & Lamkin mechanism could be expected for the unloaded blade, due to the fact that in the absence of separation, viscous effects reduce quickly the strength of the vortex during its passage over the airfoil.

A serious effort is under way to quickly unload the leading blade of a helicopter rotor for a short phase of the periodic motion, in order to reduce the strength of the tip vortex which is about to interact with a trailing blade. It was expected that a weakened vortex will not produce large pressure fluctuations on a blade that follows. Indeed Marcolini et al. (1995) proved that the sound level measured beneath such a rotor can be reduced by 4 dB. The present findings indicate that alternatively, we could temporarily unload the blade when the interaction is imminent. Another option to alleviate the detrimental effects of BVI might be to mount a small flat plate above the leading edge of the blade,
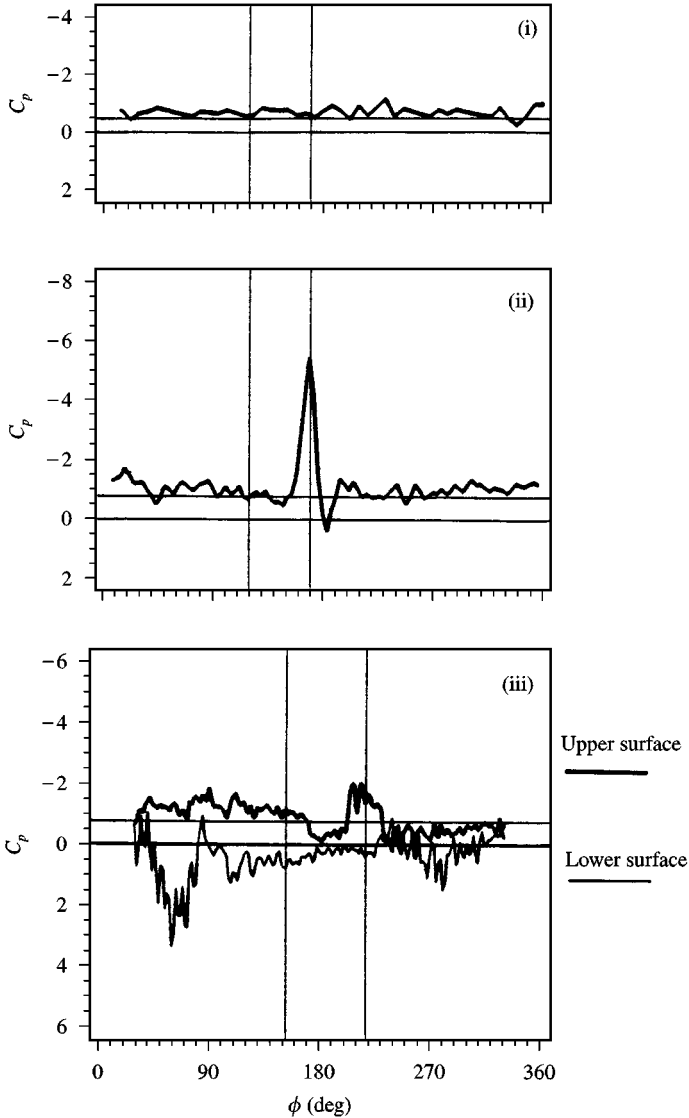
Figure 14(c). Surface pressure coefficients versus phase for $x/c = 0.3$.

in order to chop the vortex which is about to interact with the blade. This would probably bring the same results with the direct collision of the vortex with the blade and therefore will cause the vortex to disintegrate. Some technical difficulties may arise in the manufacturing of such devices, but these considerations are beyond the scope of the present publication.

4. CONCLUSIONS

We found that a vortex skimming over a blade at zero incidence does not induce separation, in agreement with the work of Gursul & Rockwell (1990), even though our vortices were much stronger than those of Gursul & Rockwell. Mapping carefully the velocity and

vorticity field over the blade, we discovered that the vortex quickly loses its strength. This cannot be explained by the inviscid effects of the vortex and its image, because such a pair would tend to propel itself downstream. The only other effect to account for the weakening of this vortex is viscosity. Indeed, a positive (counterclockwise) vortex on the upper surface of the blade induces positive velocity on the wall and tends to accelerate the flow and thereby increase the shear stresses within the boundary layer.

We then discovered that a vortex skimming over a blade at incidence induces separation and the creation of a separation bubble. This is because the flow inclination due to the vortex is added to the blade angle of attack. The phenomenon is reminiscent of unsteady stall, except that now this characteristic behavior is confined to the leading-edge region. The positive circulation in the separation bubble is comparable in magnitude to the circulation in the disturbing vortex. The two structures propagate together over the chord of the blade. Two counter-rotating vortices are perfectly compatible with each other and induce a linear motion to themselves, in this case in the downstream direction. Moreover, now the sense of induced motion near the wall is against the oncoming stream and therefore leads to reduced shearing stresses. This explains why the pair propagates without losing its character or its strength.

Finally, in the case of direct encounter with a blade at incidence, we found that the vortex breaks in two and soon disintegrates into smaller random structures. Gursul & Rockwell observed a similar behavior when they allowed weaker vortices to interact with a rounded leading edge. What mechanism leads to a total loss of coherence of the vortices is not known. The vortical structures approaching the blade nose are turbulent, but vorticity is grouped in annular rings which, if phase averaged, give the appearance of a well-ordered structure. Apparently, this structure is very unstable, because when it collides with the blade nose, it loses its identity and breaks down to many smaller structures. Swirydczuk *et al.* (1993) found that a similar effect is observed if a vortex encounters a thin flat plate, no longer than one fourth of its core.

The case of a counterclockwise vortex skimming below the blade was not tested but should not create as violent an interaction, because its ability to increase locally the apparent angle of attack is reduced. The effect of clockwise vortices should be innocuous, because they induce lower angles of attack and therefore effectively unload a blade.

The power of the present method of investigation allows us to examine the pressure patterns on the wall and follow their temporal evolution in parallel with the events described above. The pressure signature of a vortex appears as a sharp pressure fluctuation on the wall. Similar signatures have been observed by many earlier investigators. We now find that for the case of a vortex skimming over a blade at zero incidence, the pressure fluctuations are displaced downstream in unison with the vortex. But the amplitude of the pressure fluctuation decreases sharply in response to the loss of strength of the vortex.

A vortex skimming over a loaded blade, i.e., a blade at incidence, gives rise to a secondary vortex and the pair negotiates the travel over the blade with negligible loss of circulation. As a result, the pressure fluctuations follow the downstream displacement of the vortices with very little loss of amplitude. In the direct encounter case on the other hand, the vortex breaks up into smaller vortices and the pressure fluctuations broaden significantly and lose their sharp peaks.

Our most significant finding therefore is that a close encounter with a loaded blade is most detrimental, because the disturbing vortex sustains its character and its strength during its interaction with the blade. Its pressure signature involves a single distinct large spike that propagates along the chord of the blade. This spike could be responsible for large structural loads and the generation of slapping sound.

We also found that the interaction is severe if the blade is loaded, i.e., if it is at an angle of attack and much weaker if the blade is not loaded. In fact, this explains why counter-clockwise rotating vortices produce more violent interactions. This is because such vortices

tend to increase the apparent angle of attack and therefore add to the loading of the blade.

This investigation sheds light to earlier observations discussed in the Introduction. It was earlier observed for example that small variations of parameters could result in drastic changes in the character of BVI. We found that a vortex approaching the immediate neighborhood of a blade could give rise to a violent interaction as it skims over the blade, inducing a secondary vortex and thereby preserving its identity and its strength. A very small change of its path, on the other hand, could lead it into a direct collision with the blade, which results in disintegration and therefore reduction of the severity of the interaction. Our measurements also explain the variations in pressure signatures. Even though approaching vortices are well ordered, their pressure signatures on a blade could be a single spike if the vortex skims the blade but consist of many low amplitude pressure fluctuations if it collides with the blade.

ACKNOWLEDGEMENTS

REFERENCES

ABBOTT, I. H. & VON DOENHOFF, A. E. 1959 *Theory of Wing Sections*. New York: Dover Publications.

BOOTH, E. R. 1986 Surface pressure measurements during low speed two-dimensional blade–vortex interaction, AIAA Paper 86-1856, Seattle, Washington.

BOOTH, E. R. 1987a Experimental observations of two dimensional blade–vortex interaction, AIAA Paper 87-2745, Palo Alto, CA, U.S.A.

BOOTH, E. R. 1987b Measurements of velocity and vorticity fields in the wake of an airfoil in periodic pitching motion. NASA TP-2780.

BOOTH, E. R. & YU, J. C. 1986 Two-dimensional blade-vortex flow visualization investigation. *AIAA Journal* **24**, 1468–1473.

BUSHNELL, D. M. 1984 Body–turbulence interaction. AIAA Paper 84-1527.

CARADONNA, F. X., LAUTENSCHLAGER, J. L. & SILVA, M. J. 1988 An experimental study of rotor-vortex interactions. AIAA Paper 88-0045, Reno, Nevada.

CHANDRASEKHARA CARR, & WILDER 1994 Interferometric investigations of compressible dynamic stall over a transiently pitching airfoil. *AIAA Journal* **32**, 586–593.

FARASSAT, F. & SUCCI, G. P. 1983 The prediction of helicopter rotor discrete frequency noise. *Vertica*, **7**, 309–320.

GRAF, H. R. & DURGIN, W. W. 1990 Measurement of the nonsteady flow field in the opening of a resonating cavity excited by grazing flow. *ASME International Symposium on Non-steady Fluid Dynamics*, Toronto, Ontario, Canada, pp. 409–416.

GURSUL, I. & ROCKWELL, D. 1990 Vortex street impinging upon an elliptical leading edge. *Journal of Fluid Mechanics* **211**, 211–242.

HARDIN, J. C. & LAMKIN, S. L. 1987a Concepts for reduction of blade-vortex interaction noise, *Journal of Aircraft*. **24**, 120–125.

HARDIN, J. C. & LAMKIN, S. L. 1987b An Euler code calculation of blade-vortex interaction noise. *ASME Journal of Vibration, Acoustics, Stress, and Reliability in Design* **109**, 29–36.

HO, C. & CHEN, S. 1981 Unsteady wake of a plunging airfoil. *AIAA Journal* **19**, 1492–1494.

IMAICHI, K. & OHMI, K. 1983 Numerical processing of flow-visualization pictures—measurements of two-dimensional vortex flow. *Journal of Fluid Mechanics* **129**, 283–311.

JONES, W. P. 1972 Vortex-elliptic wing interaction. *AIAA Journal* (*Technical Notes*), **10**, 225–227.

KAYAKAYOGLU, R. & ROCKWELL, D. 1985 Vortices incident upon a leading edge: instantaneous pressure fields. *Journal of Fluid Mechanics* **156**, 439–461.

KOROMILAS, C. A., & TELIONIS, D. P. 1980 Unsteady laminar separation: an experimental study. *Journal of Fluid Mechanics* **97**, 347–384.

LEE, D. J. & ROBERTS, L. 1985 Interaction of a turbulent vortex with a lifting surface. AIAA Paper 85-0004.

LEE, D. J. & SMITH, C. A. 1987 Distortion of the vortex core during blade–vortex interaction. AIAA Paper 87-1243, Honolulu, Hawaii.

LEE, D. J., KIM, Y. N. & PARK, J. H. 1990 Numerical study of vortex-wedge interaction. AIAA Paper 90-3918, Tallahassee, FL, U.S.A.

MARCOLINI, M. A., BOOTH, Jr., E. R., TADGHIGHI, H., HASSAN, A. A., SMITH, C. D. & BECKER, L. E. 1995 Control of BVI noise using an active trailing edge flap. *American Helicopter Society*, *Vertical Aircraft Design Conference*, San Francisco, CA, U.S.A.

MARTIN, R. M. & SPLETTSTOESSER, W. R. 1987 Acoustic results of the blade-vortex interaction acoustic test of a 40-percent model rotor in the DNW. AHS Specialists' Meeting on Aerodynamics and Acoustics, Arlington, TX, U.S.A.

MATHIOULAKIS, D. S., KIM, M. J., TELIONIS, D. P. and MOOK, D. T. 1985 On the wake of a pitching airfoil. AIAA Paper 85-1621, Cincinnati, OH, U.S.A.

MATHIOULAKIS, D. S. & TELIONIS, D. P. 1987 Velocity and vorticity distribution in periodic separation flow. *Journal of Fluid Mechanics*, **184,** 303–333.

MATHIOULAKIS, D. S. & TELIONIS, D. P. 1989 Pulsating flow over an ellipse at an angle of attack. *Journal of Fluid Mechanics* **201,** 99–121.

MEIER, G. E. A. & TIMM, R. 1985 Unsteady vortex airfoil interaction. AGARD CP-386.

PANARAS, A. G. 1987 Numerical modeling of the vortex/airfoil interaction. *AIAA Journal* **25,** 5–11.

PESCE, M. M. 1990 Unsteady Pressure and vorticity fields in blade-vortex interactions. M. S. Thesis, Virginia Polytechnic Institute & State University, Blacksburg, VA, U.S.A.

PESCE, M. M., WILDER, M. C. & TELIONIS, D. P. 1991 The evolution of pressure and vorticity fields during blade-vortex interaction. *Proceedings of the Second World Conference on Experimental Heat Transfer*, *Fluid Mechanics and Thermodynamics*, Dubrovnik, Yugoslavia.

POLING, D. R. 1985 Airfoil response to periodic disturbances- the unsteady Kutta condition. Ph.D. Dissertation, Virginia Polytechnic Institute & State University, Blacksburg, VA, U.S.A.

POLING, D. R. and TELIONIS, D. P. 1986 Airfoil response to periodic disturbances-the unsteady Kutta condition. *AIAA Journal* **24,** 193-199.

POLING, D. R., DADONE, L., WILDER, M. C. & TELIONIS, D. P. 1988 Two-dimensional interaction of vortices with a blade. AIAA Paper 88-0044, Reno, Nevada.

POLING D. R., DADONE, L. & TELIONIS, D. P. 1989 Blade-vortex interaction. *AIAA Journal*, **27,** 694–699.

POLING, D. R., WILDER, M. C. & TELIONIS, D. P. 1991 Fundamental research in helicopter rotor blade-vortex interaction modeling. *Proceeding of the 47th Annual Forum of the American Helicopter Society*, Phoenix, AZ, U.S.A., pp. 421–433.

ROCKWELL, D. 1984 Unsteady loading of leading-edges in unstable flows: an overview. AIAA Paper 84-2306.

ROCKWELL, D. & KNISELY, C. 1979 The organized nature of flow impingement upon a corner, *Journal of Fluid Mechanics* **93,** 413–432.

SOHN, D. & ROCKWELL, D. 1987 Vortex Interaction with a Leading Edge of Finite Thickness, NASA Contractor's Report, NASA-CR-192341.

SPLETTSTOESSER, W. R., SCHULTZ, K. J. & MARTIN, R. M. 1987 Rotor blade-vortex interaction impulsive noise source identification and correlation with rotor wake predictions. AIAA Paper 87-2744.

SRINIVASAN, G. R. & MCCROSKEY, W. J. 1993 Euler calculations of unsteady interaction of advancing rotor with a line vortex. *AIAA Journal* **31,** 1659–1666.

STRAUS, J., RENZONI, P. & MAYLE, R. E. 1990 Airfoil pressure measurements during a blade vortex interaction and a comparison with theory. *AIAA Journal* **28,** 222–228.

SWIRYDCZUK, J. 1990 A visualization study of the interaction of a free vortex with the wake behind an airfoil. *Experiments in Fluids* **9,** 181–190.

SWIRYDCZUK, J., WILDER, M. C., & TELIONIS, D. P. 1993 The interaction of coherent vortices with thin flat plates. *ASME Journal of Fluids Engineering* **115**, 590–596.

TELIONIS, D. P., MATHIOULAKIS, D. S., KIM, B. K. & JONES, G. S. 1986 Calibration of the ESM water tunnel. VPI & SU Engineering Report No. VPI-E-86-23.

TELIONIS, D. P. & WILDER, M. C. 1988 Progress report on the interaction of vortices with a fixed blade. VPI & SU Engineering Report No. VPI-E-88-2.

THOMPSON, T. L., KWON, O. J., KEMNITZ, J. L., KOMERATH, N. M. & GRAY, R. B. 1987 Tip vortex core measurements on a hovering model rotor, AIAA Paper 87-0209, Reno, Nevada.

WIDNALL, S. 1971 Helicopter noise due to blade–vortex interaction. *Journal of the Acoustical Society of America* **50,** 354–365.

WILDER, M. C. 1992 Airfoil-vortex interaction and the wake of an oscillating airfoil. VPI & SU, Ph.D. dissertation, Blackburg, VA, U.S.A.

WILDER, M. C., PESCE M. M. & TELIONIS, D. P. 1990 Blade-vortex interaction experiments - velocity and vorticity fields. AIAA Paper 90-0030, Reno, Nevada, U.S.A.

WU, J. C., SANKAR, N. L. & HSU, T. M. 1985 Unsteady aerodynamics of an airfoil encountering a passing vortex. AIAA Paper 85-0203.

WILDER, M. C., MATHIOULAKIS, D. S., POLING, D. R., & TELIONIS, D. P. 1996 The Formation and internal structure of coherent vortices in the wake of a pitching airfoil. *Journal of Fluids and Structures* **10**, 3–20.

ZIADA, S. & ROCKWELL, D. 1982 Vortex-leading-edge interaction. *Journal of Fluid Mechanics.* **118**, 79–107.

APPENDIX: NOMENCLATURE

|	
c	chord length of target airfoil
c_g	chord length of pitching airfoil
C_p	pressure coefficient, see equation (9)
d	vortex core diameter
Δx	grid size in x direction
Δy	grid size in y direction
Δh	vertical displacement of two airfoils
f	frequency
N	number of samples
M	number of time records
p	static pressure
p_∞	static pressure at the upper left corner of measurement
k	reduced frequency, $\omega c/2U_\infty$
T	period
U_d	drifting velocity of disturbance
U_∞	free stream velocity
x, y	cartesian coordinates—see Figure 2
α	angle of attack
Γ	circulation of disturbing vortex
Γ_b	bound circulation
Γ_s	sectional circulation, equation (4)
μ	viscosity
ρ	density
ϕ	phase angle
Ω	vorticity
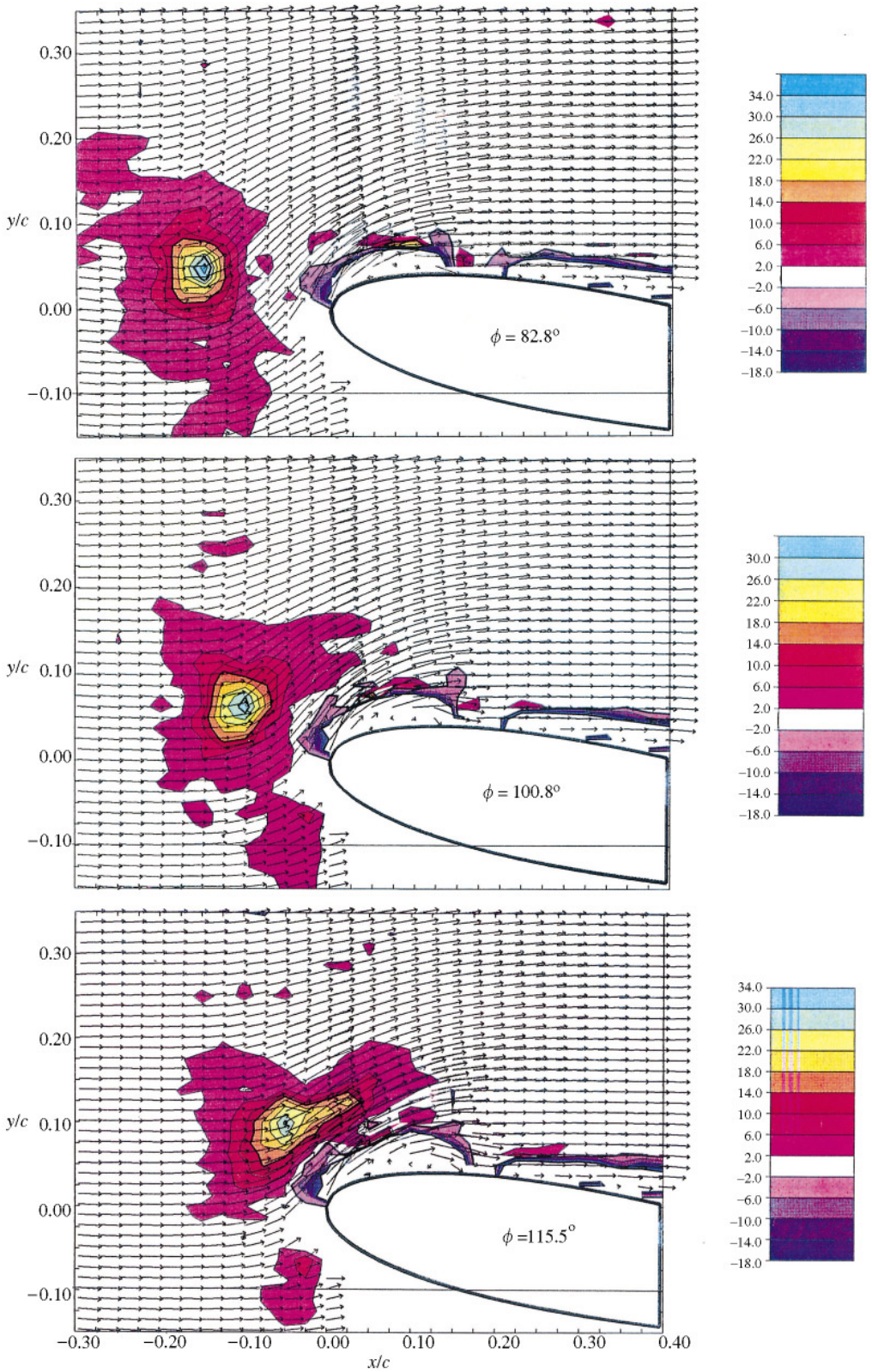
Figure 9(a). Velocity vectors and vorticity contours for $\alpha = 10°$ and $\Delta h = 0.1c$ for $\phi = 82.8°$, $100.8°$ and $115.5°$.
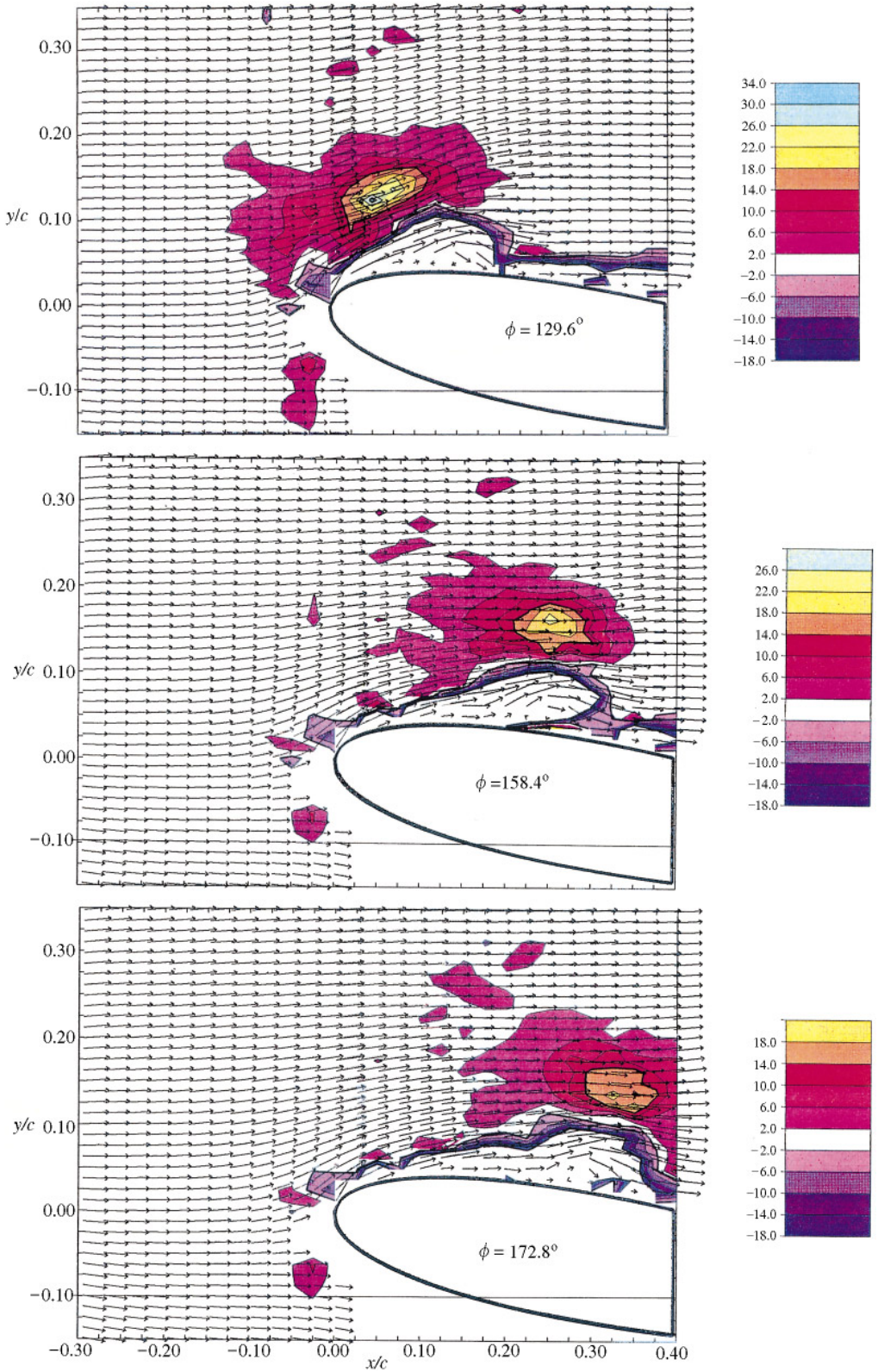
Fig. 9(b). Velocity vector and vorticity contours for $\alpha = 10°$ and $\Delta h = 0.1c$ for $\phi = 129.6°$, $158.4°$ and $172.8°$.